Frequent new particle formation events in the Indo-Gangetic Plain occur under reduced condensation sink but are obscured by air mass heterogeneity

Gaurav K. Srivastav[1,2], Aasif A. Wagay[1], Janne Lampilahti[3], Jaswant Rathore[1], Ravi K. Kunchala[1], Dilip Ganguly[1], Markku Kulmala[3], Tuukka Petäjä[3], Pauli Paasonen[3], Roseline C. Thakur[3*], Shahzad Gani[1,3*]

[1]Centre for Atmospheric Sciences, Indian Institute of Technology Delhi, New Delhi, India.
[2]India Meteorological Department, Ministry of Earth Sciences, Government of India.
[3]Institute for Atmospheric and Earth System Research/Physics, University of Helsinki, Helsinki, Finland.

Correspondence to: shahzadgani@iitd.ac.in; roseline.thakur@helsinki.fi

Abstract. New particle formation (NPF) is a major source of atmospheric aerosols and cloud condensation nuclei, influencing climate and air quality. In highly polluted regions such as the Indo-Gangetic Plain (IGP), where precursor concentrations and condensation sinks are among the highest globally, NPF remains poorly constrained due to limited observations of particles and ions in the sub–10 nm size range.

Here, we investigated the occurrence and growth of NPF at a suburban IGP site (CAS-AO, Sonipat, Haryana), during May-December 2023 using ion (0.8–42 nm) and particle (2.5–42 nm) measurements together with meteorological data. NPF events were frequent during summer, occurring on 30 of 35 valid days in May-June (86 %), and were much less frequent during the winter/post-monsoon period, with 20 out of 73 valid days (28 %). The weak seasonal variability of ion concentrations relative to nucleation-mode particles suggests that particle survival and growth were strongly modulated by condensation sink, meteorology, and air-mass heterogeneity. The median daily condensation sink during 06:00–12:00 LT was lower on event days than on non-event days (0.0095 vs 0.0292 s^{-1}). Particle growth rates increased with size, from 14.7 nm h^{-1} in the 3–7 nm range to 19.0 nm h^{-1} in the 7–20 nm range, indicating size-dependent growth.

In this high-background setting, pollution plumes and meteorological variability intermittently mask or distort NPF signals, limiting the direct applicability of both visual and automated classification methods and growth rate estimation methods. Our observations highlight that careful application and improvement of data analysis methods, along with precursor gas measurements, are required to better constrain nucleation processes by avoiding methodological sensitivity due to the complexity of aerosol dynamic processes in multi-source, high-condensation-sink environments, such as IGP.

1. Introduction

Aerosols affect the global radiation balance by scattering sunlight and altering cloud properties. They originate from natural (e.g., volcanoes, sea spray) and human sources (e.g., industry, transport) and occur as primary (directly emitted) or secondary (formed via atmospheric reactions) particles (Hinds and Zhu, 2022). Aerosol sizes range from sub–2 nm atmospheric clusters (particles) and small ions, to coarse particles reaching hundreds of micrometres (Kulmala et al., 2024; Tomasi and Lupi, 2017).

New particle formation (NPF) is the atmospheric process by which low-volatility vapours form molecular clusters that can grow into detectable aerosol particles. Freshly formed particles typically appear first at diameters of about 1.5–2 nm and may subsequently grow into the nucleation and Aitken modes if condensable vapours are sufficient and losses to pre-existing particles are limited. Charged sub–10 nm particles and ions influence atmospheric electrical properties and can provide early information on cluster formation and growth.

Atmospheric observations and model studies show that NPF followed by growth can contribute substantially to atmospheric particle number concentrations, while its contribution to cloud condensation nuclei (CCN) depends on whether newly formed particles grow to CCN-relevant sizes (Gordon et al., 2017; Kerminen et al., 2018). Both contributions vary strongly among sites, seasons, and background aerosol conditions. During an NPF event, the observed concentration in a fixed nucleation-mode size interval can increase as the growing mode passes through that interval, even though the total number in a growing particle population may decrease because of coagulation and dilution.

The Indo-Gangetic Plain (IGP), spanning parts of India, Pakistan, Bangladesh, and Nepal, supports intensive agriculture through its fertile alluvial soil and major river systems. It is a densely populated region characterised by complex meteorological factors, and faces pressing challenges related to rapid urbanisation and industrial growth, resulting in significant air pollution levels. The region not only witnesses extreme levels of air pollution in winters but also experiences anomalies in precipitation, alternating weather during the Indian summer monsoon period and periodic impact of western disturbances. IGP, characterised by a rich mix of industrial and anthropogenic activities, presents a diverse array of aerosol sources. Increasing aerosol loading, along with a prominent role of precursors such as NH_3 (primarily from agricultural emissions), and discernible upward trend in SO_2 and NO_x are likely to enhance the potential for secondary aerosol formation and further complicate atmospheric processes (Chutia et al., 2022; Gani et al., 2019; Pawar et al., 2023; Singh et al., 2023; Wang et al., 2020).

However, current knowledge of these processes in the IGP remains limited because previous studies have largely relied on the Scanning Mobility Particle Sizer (SMPS) and similar instruments optimised for larger particle diameter (typically above 10 nm), which often miss the dynamics of particles and ions in the 3–10 nm size range (Kanawade et al., 2022). Furthermore, many existing observations are conducted over short time durations, making it difficult to fully understand the seasonal variability of NPF and sub–10 nm particle dynamics in the IGP. These factors stress the need to study the nuances of secondary particles and NPF events particular to this region (Gani et al., 2019; Kanawade et al., 2022; Laakso et al., 2006; Sebastian et al., 2022).

Several mechanisms have been proposed to explain atmospheric NPF. Classical pathways include binary water–sulfuric acid nucleation, ternary water–sulfuric acid–ammonia nucleation, and ion-induced nucleation (Kirkby et al., 2016; Kulmala et al., 2004; Kulmala and Laaksonen, 1990; Seinfeld, 2016). More recent studies show that the

atmospheric mechanism is often more complex and can involve additional stabilising vapours, including amines, highly oxygenated organic molecules, and other low-volatility compounds, with their relative importance depending on temperature, emissions, and background aerosol loading (Kulmala et al., 2023). In warm and polluted environments such as the IGP, pure sulfuric-acid–ammonia pathways are therefore unlikely to provide a complete explanation, and stronger bases, organic vapours, and high pre-existing aerosol sinks may all influence whether newly formed clusters survive and grow.

In this study, we investigate the temporal variability of size-resolved atmospheric ions and NAIS-measured particle concentrations at the IGP site and examine their relationships with concurrent meteorological parameters. From the available observations, we identify NPF event days using complementary classification methods and determine their frequency, growth rates, and formation-rate case-study estimates. Derived quantities that require larger particle sizes, including condensation sink, coagulation sink, and formation rate, are restricted to periods with concurrent NAIS and SMPS measurements.

2. Material and methods

2.1 Observation site:

We analyse the temporal variability of size-resolved ions and NAIS-measured particle concentrations using instrumental facilities established at the Atmospheric Observatory - Centre for Atmospheric Sciences (CAS-AO) (Rathore et al., 2025). The site is in Sonipat district, Haryana, India (28.99 degrees N, 77.01 degrees E; ~125 m a.s.l.). It is a suburban site located ~65 km from the IIT Delhi main campus and ~10 km northwest of the northern boundary of Delhi. Agricultural land surrounds the site, while National Highways 44 and 34 intersect approximately 500 m from the sampling inlet. These highways represent the dominant nearby source of traffic-related emissions, in addition to advected regional sources. Industrial chimneys are also located beyond the intersecting highways. Residential areas lie approximately 300-400 m from the site and may contribute diesel-generator and household emissions. Small water bodies, including ponds and fish farms, are present nearby, and the Yamuna River flows within approximately 10 km of the site, potentially influencing local humidity and vapour precursors for particle formation and growth.

Figure 1 illustrates the measurement site's geographical context from Google Maps, including a zoomed-in view highlighting nearby roads and infrastructure (left), and a broader view showing its position within India (right). From a meteorological perspective, the CAS-AO acts as a receptor for air masses originating from upwind regions, including parts of the Middle East, Pakistan, and northern India. Its location, combined with proximity to major highways, agricultural activity, industrial sources, and residential areas, makes it well suited for investigating the interplay between local emissions, regional transport, and atmospheric processing of aerosols under subtropical conditions. The dataset used for the present paper is from May 2023 to Dec 2023.

2.2 Instrumentation

In this study, we used a Neutral Cluster and Air Ion Spectrometer (NAIS) and a Scanning Mobility Particle Sizer (SMPS). We operated the instruments on two independent sampling lines. We measured meteorological parameters using an Automatic Weather Station (AWS) installed on the rooftop of the same building (I-Tech Park building IIT

Delhi's Sonipat campus). Unless otherwise specified, all diameters referenced in this study refer to mobility diameters. A brief description of the instruments is as follows:

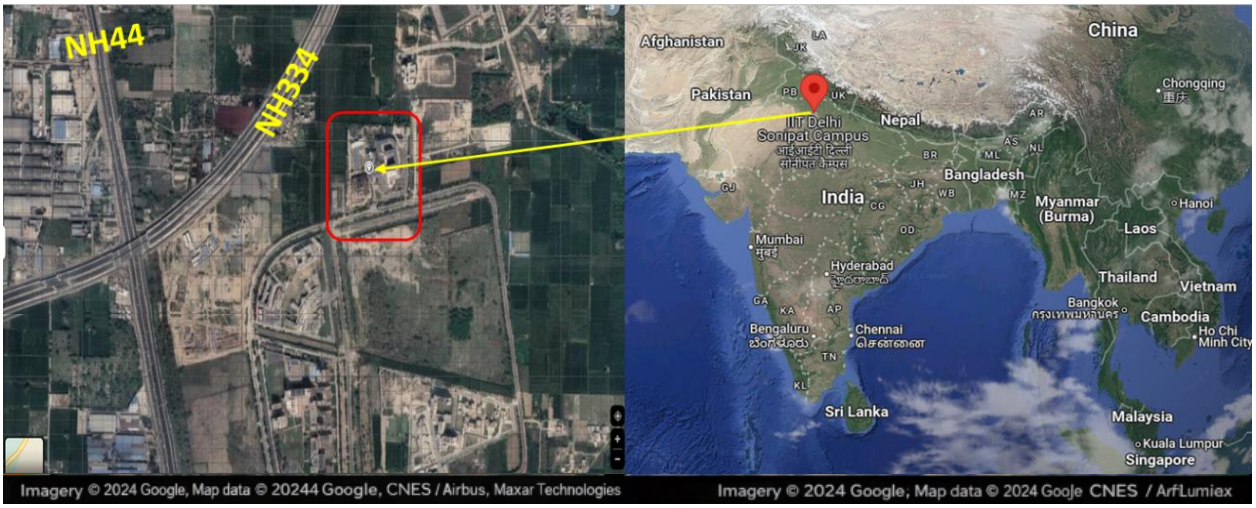

Figure 1: Map showing the location of the CAS-AO, including local surroundings (left) and its position within India (right). Base map from Google Maps (Maps data © 2024 Google, retrieved 15 January 2024).

2.2.1 Neutral Cluster Air Ion Spectrometer (NAIS)

The Neutral Cluster and Air Ion Spectrometer (NAIS) measures particle number size distributions (PNSDs) of total particles (2–42 nm) and charged particles/ions (0.8–42 nm), making it particularly suitable for studying atmospheric ions and particles (Mirme and Mirme, 2013). It employs parallel differential mobility analysis using two identical cylindrical DMAs, with one channel for positive ions and the other for negative ions together with a pre-conditioning unit that charges particles via unipolar ionization (corona discharge) before they enter the DMAs. This allows the instrument to resolve both naturally charged ions and neutral particles within its size range. Measurements of neutral clusters below ~2 nm carry significant uncertainty due to electrometer noise, corona-charging artefacts, and enhanced diffusional losses, particularly under high particle loadings during winter, which may affect absolute number concentrations (Kulmala et al., 2007, 2012). Above 2 nm size range, its sensitivity is constrained by the electrometers' detection limits and the corona charger, which restricts the smallest measurable concentrations and particle sizes (Manninen et al., 2011; Wagner et al., 2016). As such, we did not incorporate sub–2.5 nm total particle data in our analysis.

The NAIS spectra were inverted by the NAIS/Airel instrument software (spectops) using the instrument-specific inverter v14.1-hrnd-elm25-chv. The measurement sequence consisted of 30 s offset, 30 s particle-mode, and 30 s ion-mode measurements, with 1- and 10-min averages saved by the instrument. The exported spectra were then post-processed by converting ion mobility distributions to diameter-based PNSDs, applying inlet-loss correction based on the Gormley–Kennedy tube-loss formulation (Gormley and Kennedy, 1949), and applying ion-mode correction following (Wagner et al., 2016). The final processed NAIS data were averaged to 5 min time resolution.

NAIS PNSD measurement uncertainties are size- and mode-dependent, and intercomparison studies have shown that air-ion spectrometer concentrations can vary between instruments and operating conditions (Gagné et al., 2011; Wagner et al., 2016). For ion-mode measurements, Wagner et al. (2016) reported that uncorrected NAIS number concentrations were underestimated by about 15–30 % below 5 nm, whereas concentrations at diameters of 19.6 nm and larger were overestimated by up to 8 %. After the Wagner et al. correction, ion concentration uncertainty can be reduced to below 10 %. In particle mode, the largest uncertainty occurs near the lower size limit because corona-generated charger ions overlap with the smallest particle sizes; particles below about 2–3 nm cannot be reliably distinguished from charger ions, and the lower detectable size can vary with environmental conditions (Manninen et al., 2011, 2016). Therefore, sub–2.5 nm NAIS total-particle data were excluded from quantitative particle analysis.

NAIS offers several advantages: it measures both charged and neutral particles, provides high time resolution for capturing rapid changes in particle concentrations, and is relatively portable, enabling use in field campaigns. At the CAS-AO, the NAIS inlet consists of a 100 cm copper tube (3 cm diameter) mounted through a laboratory wall at ~5 m above ground level. Oriented downward without sharp bends, the downward inlet minimises interference from raindrops. Unless stated separately, "total particles" refers to the NAIS particle-mode measurement (i.e., the number size distribution of all particles regardless of natural charge state, following unipolar charging), reported over the 2.5–42 nm range used in this study; "ions" refers separately to the NAIS ion-mode measurement of naturally charged particles over 0.8–42 nm. The two channels are reported separately throughout this study unless explicitly stated as combined.

2.2.2 Scanning Mobility Particle Sizer (SMPS)

The SMPS was used to measure PNSDs at larger particle diameters (Aalto et al., 2001). The larger-diameter part of the PNSD was used, together with NAIS data where available, to calculate the condensation sink. SMPS consists of an electrostatic classifier (TSI model 3082), a differential mobility analyser (DMA; TSI model 3081), an X-ray aerosol neutralizer (TSI model 3088), and a condensation particle counter (CPC; TSI model 3750). The SMPS operates on the monotonic relationship between electrical mobility and particle size for singly charged particles. The neutralizer provides a stable charge distribution by bipolar charging. Then the classifier separates out particles of targeted diameter range (bins) by varying the voltage where monotonic relationship between electrical mobility and particle size of single-charge particles is used (Stolzenburg and McMurry, 2018; Tammet, 1995). The classified sample via differential mobility analyser is further sent to CPC and the size distribution is determined (Kangasluoma et al., 2020; Stolzenburg and McMurry, 2018). Typical SMPS uncertainties arise from assumptions in the bipolar charge distribution (~5–10 % for particles in the 20–100 nm range), finite DMA transfer function width and inversion-related effects (resulting in a sizing uncertainty of ~5–10 %), flow rate calibration (±2–5 %), and CPC counting efficiency (>95 % above the lower detection limit, with reduced efficiency close to the cutoff diameter). The combined relative uncertainty in PNSD is typically on the order of 10–20 % across the 12–570 nm size range, increasing toward the lower and upper size extremes (Johnson et al., 2020; Kangasluoma et al., 2020; Leppä et al., 2017). The raw SMPS scans were inverted using TSI Aerosol Instrument Manager software (AIM version 11.03.00). The exported PNSD covered approximately 12–570 nm, with 128 channels per decade, a 120 s scan time, and a 4 s retrace time.

During concurrent operation, the NAIS and SMPS were compared in their overlapping size range of approximately 12–42 nm. The instruments captured similar temporal variability, but absolute concentrations differed because of differences in sampling lines, charging and inversion assumptions, detection principles, and particle losses near the lower SMPS and upper NAIS overlap region. For analyses requiring a continuous NAIS–SMPS PNSD, day-specific multiplicative scale factors were derived from the median concentration ratio in the overlapping size range and applied before merging. The NAIS-based event classification was not affected by this scaling.

2.2.3 Automatic Weather Station (AWS)

The AWS provides real-time measurements of meteorological parameters at 5-minute resolution (CIMO Guide No.8, WMO, 2017). The station integrates sensors connected to a digital logger. Measured parameters include air temperature, wind speed, wind direction, relative humidity, and solar radiation. The sensor-parameter pairs are: thermometer for temperature, anemometer for wind speed, wind vane for wind direction, capacitive sensor for relative humidity, barometer for atmospheric pressure, and pyranometer for solar radiation.

2.3 Methodology, conventions and data processing

In this study, the seasons are demarcated according to specific time frames. Winter spans December-February, spring March-April, summer May-June, monsoon July-September, and autumn October-November, following the seasonal grouping used in previous Delhi aerosol analyses (Gani et al., 2020). We divide the diurnal cycle into two time periods: day (6-18 h) and night (18-6 h). All temporal references throughout this study are expressed in local time (LT), specifically in Indian Standard Time (IST; GMT+05:30). This structured approach to seasonal and temporal divisions facilitates a more comprehensive understanding of the data and enables us to draw meaningful comparisons across different time frames. We have used the ions and total particles data from NAIS negative channel.

Data coverage for the different instruments and derived quantities is summarised in Fig. S1. Although the overall measurement period extended from May to December 2023, the number of valid days available for individual analyses differed because of instrument interruptions, missing data periods, precipitation-affected ion measurements, and gaps during the daytime growth window used for event classification. The NAIS-based NPF classification was performed using 108 valid NAIS days. SMPS measurements usable for the concurrent NAIS-SMPS analysis were available for a limited subset of the campaign (26 days), mainly during August-November 2023.

Data observed from AWS is presented in supplementary Fig. S2 which shows the typical seasonal diurnal variability of key meteorological parameters with significant variations in temperature (T), relative humidity (RH), wind speeds, and wind direction throughout the year. Winter (December–February) is characterised by low temperatures (~2–18°C), high relative humidity (~35–95 %), and low wind speeds (~1.5–4 m s^{-1}). During winter, the site frequently experiences shallow atmospheric boundary layers (depth < 100 m), particularly at night and in the morning. In contrast, the summer months (April to June) are marked by intense heat (T ~ 25 to 40 °C) and dry conditions (RH ~ 30–70 %). The monsoon season, spanning from July to mid-September, brings episodic heavy rainfall to the majority of the IGP. This period is characterised by slightly lower temperatures (T ~ 20 to 35 °C) compared to the summer. There may be some occurrence of relatively high temperatures, but mostly these are infrequent. Notably, the winds predominantly come from the northwest throughout most of the year, but during the

summer and monsoon, they shift to south during the nighttime. Conditions unfavourable for atmospheric dispersion, such as low wind speeds, shallow boundary-layer heights, and stagnant high-pressure periods, often enhance pollutant accumulation, leading to exceptionally high $PM_{2.5}$ concentrations (Guttikunda and Gurjar, 2012; Trivedi et al., 2014).

Researchers have proposed different classification frameworks in the literature to classify the observed particle number size distribution (PNSD) and identify the NPF events. Classification of PNSD is essential because it helps understand the frequency and characteristics of NPF events and enables quantification of particle formation and growth rates. However, the interpretation of NPF frequency is not solely a property of the atmospheric conditions but also depends on the choice of detection methodology, instrumentation sensitivity, and the specific classification logic applied.

One of the earliest systematic and widely adopted approaches for classifying NPF events was introduced by Dal Maso et al. (2005). This scheme is based on visual inspection of daily PSD and identifies an event when a distinct nucleation mode appears, persists for more than 1 h, and shows continuous growth toward larger diameters. Events are further categorised according to whether growth and formation rates can be reliably quantified: Class Ia denotes well-defined events, Class Ib denotes events that are visible but less clear than Class Ia, and Class II denotes less distinct events with weaker growth signatures. Days without such features are classified as non-events. This classification involves visual interpretation and is therefore inherently subjective and time intensive, but it remains a useful first-step diagnostic approach because it provides a structured and physically consistent way to separate event from non-event days in long-term aerosol datasets.

In the present study, we adopted the Dal Maso et al. (2005) classification framework with minor adjustments suited to our dataset. Distinguishing between subcategories Class Ia and Class Ib was not feasible, as most event-days exhibited an early and sharp burst of particles that obscured a clear separation between very strong and moderately strong events. Therefore, we grouped all clearly observable and well-developed growth events into Class I, while days showing NPF signatures under background influence or with less distinct growth were classified as Class II. Days without identifiable nucleation and growth were categorised as non-events. Days containing data gaps longer than 30-minutes were excluded. Days with even 30-minutes missing data during the critical daytime growth period were also discarded to avoid biased classification.

Another classification method, Dada et al. (2018) detects initial cluster formation signals by searching periods with elevated 2–4 nm ion concentrations and investigates NPF signals using periods with elevated 7–25 nm particle concentrations. Based on daily PNSD, the method classifies days into four categories: Regional Events: Elevated period observed in 2–4 nm ions and subsequently in 7–25 nm particles (local formation with growth), Ion Bursts: 2–4 nm ions present but no elevated concentration observed in larger particles, Transported events: 7–25 nm particles present without local ion formation (carried from elsewhere), and the Non-Events: Neither sufficient ion nor particle elevated concentration periods detected. This automated method identifies exact start, peak, and end times of events while excluding precipitation periods that interfere with ion measurements.

We applied this classification to observations from CAS-AO in a slightly modified way. Using monthly mean particle number concentrations above 12 nm, we observed a substantial contribution from background aerosol loading and instrument noise, particularly during the winter months, making it difficult to isolate the NPF growth

signal in the full 7-25 nm range prescribed by Dada et al. (2018). Therefore, we restricted the particle-growth criterion to the 7-12 nm range. This site-specific adaptation improves robustness for the present high-background dataset, but it also means that the resulting classes are not directly equivalent to studies applying the standard 7-25 nm Dada et al. bounds.

An alternative and recently developed technique for analysing NPF events is the nanoparticle ranking analysis method proposed by Aliaga et al. (2023). This approach offers a quantitative and objective framework to evaluate the likelihood and strength of NPF events by examining daily changes in particle number concentrations within the 2.5–5 nm size range ($\Delta N_{2.5–5}$). This parameter is calculated from smoothed time series by contrasting background (night-time) and active (daytime) periods, yielding a single metric for each day that reflects the intensity of potential NPF. The days are then ranked according to this parameter and grouped into percentile classes or Gaussian modes of $\log(\Delta N_{2.5–5})$ which allows the probability and strength of NPF to be examined continuously rather than via a binary event/non-event classification. This method produces a continuous variable that facilitates the probabilistic assessment of both strong and weak NPF occurrences.

In this study, we applied the nanoparticle ranking analysis following the framework of (Aliaga et al., 2023) to characterise NPF behaviour at CAS-AO. The ranking parameter was derived from the 3–5 nm particle number concentration (the lowest reliable size bin of our instrument), calculated as the difference between the daytime maximum concentration (6–18 h LT) and the nighttime median background concentration (21–6 h LT). This size range avoids contamination from the continuous molecular cluster mode at the lower end and reduces influence from primary anthropogenic emission sources, including traffic, at the upper end. A 2-hour rolling median smoothing was applied prior to the calculation to reduce short-term variability. The resulting $\Delta N_{3–5}$ values were ranked across the full observational period and grouped into 5 % percentile intervals.

Growth rate (GR) is defined as the temporal rate of change of particle diameter (dD_p/dt), expressed in nm h^{-1}, representing the speed at which newly formed particles increase in size during growth events. In this study, GR was estimated using two independent approaches: maximum concentration method (using Gaussian function fitting) and appearance time method (using sigmoid function) (Kulmala et al., 2012). We have used particle number concentrations with size ranges (3–7 nm, and 7–20 nm). Particle number concentration has been smoothed using a rolling median filter to avoid noisy signals and temporary fluctuations. For the maximum concentration approach, the temporal evolution of each size bin concentration was fitted using a least-squares Gaussian function to determine the peak time. The growth rate was then calculated by performing a linear regression between peak times and corresponding particle diameters, expressed in nm h^{-1}. For the appearance method, the rising portion of each size-bin concentration curve was fitted with a sigmoid function to determine the 50 % appearance time (t_{50}). Growth rates were derived by regressing t_{50} values against particle diameter. The resulting growth rates distributions were visualised using box-and-strip plots to represent central tendency, spread, and event-to-event variability while preserving individual data points. Before fitting, we examined the distribution's evolution over time to identify the window that represents the growth. Each fit and its peak-specific diameter range (in both categories) were reviewed to confirm that a representative time was reliably detected.

For GR estimation, the modified Dal Maso et al. (2005) classification was used to identify candidate event days. Class I and Class II days were considered because both categories can contain visually traceable growth features.

Each candidate event day was then inspected individually. The nominal 3–7 nm and 7–20 nm intervals were used as initial search ranges, but the full interval was not imposed if part of the range was affected by noise, weak mode separation, plume-like variability, or discontinuous concentration enhancements. Instead, different contiguous sub-ranges and fitting windows within the nominal intervals were tested, and GR was calculated only for the portion that showed a coherent diameter–time growth pattern representative of NPF. Days or size intervals dominated by short-lived bursts or pseudo-growth signals were excluded from the GR statistics. This procedure yielded 17 NAIS event days suitable for at least one GR estimate.

The condensation sink (CS) was calculated from the aerosol PNSD following the diameter-based formulation described by (Ezhova et al., 2018; Pirjola et al., 1999): $CS = 2\pi D\sum\beta(D_p)D_pN(Dp)$, where D is the vapour diffusion coefficient, D_p is particle diameter, $\beta(D_p)$ is the transition-regime correction factor, and $N(D_p)$ is the particle number concentration in each size bin. The PNSD were obtained by combining NAIS measurements below 20 nm with SMPS measurements above 20 nm, resulting in a continuous size spectrum spanning the nucleation and accumulation modes for concurrent-instrument days.

For the event/non-event CS comparison, daily CS values were summarised as the median CS during 06:00-12:00 LT. This morning window was selected to represent the pre-onset, onset, and early-growth period of NPF while avoiding later afternoon boundary-layer accumulation and local emission effects. Of the 26 concurrent NAIS-SMPS days, 11 were NAIS event days and 15 were NAIS non-event days; two of the event days (6 September and 16 October 2023) were treated as disagreement/ambiguous cases because the SMPS particle size distribution did not support a clean event-day interpretation, leaving 9 event days and 15 non-event days for the condensation-sink comparison. Condensation sinks were therefore calculated only from these 9 event days and 15 non-event days, because particles outside the NAIS size range contribute substantially to these sinks. For CS calculations, NAIS particle data were used up to 20 nm and SMPS data above 20 nm, producing a merged PNSD of approximately 2.5-570 nm for concurrent-instrument days.

The particle formation rate (J) represents the rate at which new particles are formed at a given size and is expressed in cm^{-3} s^{-1}. Formation rates were determined for both 3 nm (J_3) and 7 nm (J_7), with the J_3 equation shown as the representative formulation. These calculations were performed only for three case-study event days with concurrent NAIS and SMPS data and sufficient data quality for dN/dt, CoagS, and the growth-out-of-range term. For these days, the SMPS was available and a usable GR could be estimated, so CoagS and J were calculated from the merged NAIS+SMPS PNSD rather than from a truncated NAIS-only distribution.

The formation rate was calculated as:

$$J_3 = \frac{dN_{3-7}}{dt} + CoagS \cdot N_{3-7} + \frac{GR}{\Delta D_p} \cdot N_{3-7} \tag{1}$$

where N_{3-7} is the particle number concentration in the 3–7 nm size range, $\frac{dN_{3-7}}{dt}$ is the temporal change in concentration, $CoagS$ is the coagulation sink representing losses due to coagulation with pre-existing particles, GR is the particle growth rate (nm h^{-1}), and ΔD_p is the width of the size interval (nm).

The first term represents the net increase in particle concentration, the second term accounts for losses due to coagulation, and the third term corrects for particles growing out of the size range. The coagulation sink was

calculated using standard coagulation theory for interactions between newly formed particles and the background aerosol population (Kulmala et al., 2012; Lehtinen et al., 2007). For the three Table 1 case-study days, this term used the combined NAIS+SMPS PNSD, covering the available particle sizes from the NAIS lower particle range to the upper SMPS range (~2.5-570 nm). To reduce the influence of short-term fluctuations and measurement noise, particle number concentrations were smoothed before calculating dN/dt. For J_3, particle sizes between 3 and 7 nm were used; for J_7, particle sizes between 7 and 20 nm were used. Formation rates were therefore calculated only for the smaller case-study subset of event days for which all required terms (CS from SMPS-NAIS data, GR from NAIS data) could be determined reliably.

3. Results and discussion

3.1 Particle and ion number concentrations

Particle and ion number concentrations measured by the NAIS at CAS-AO exhibit pronounced diurnal and seasonal variability (Fig. 2). NAIS-measured particle concentrations in Fig. 2(a) show clear daytime enhancements during May-June, while these features become more episodic and delayed during August-September. In contrast, October-December exhibits weak and poorly structured diurnal variability, with no clearly defined growth patterns.

In May-June, particle growth typically begins early in the day (around 6 h LT), while in August-September the onset appears somewhat later and more variable. This seasonal contrast is consistent with stronger photochemical activity and more favourable dilution conditions during the warmer months, whereas colder months are more often affected by high background aerosol loading and weaker boundary-layer mixing.

Ion number concentrations in Fig 2(b) display broadly similar but generally more subdued features. Distinct midday enhancements are primarily observed during May and June, while distributions become progressively more uniform toward winter. Overall, the warmer months show clearer and more continuous growth signatures, indicating a strong seasonal modulation of NPF-related processes at the site. The smallest diameter ranges (below ~3 nm for total particles and ~2 nm for ions) are influenced by corona-generated charger ions and instrumental noise. Concentrations above 12 nm are dominated by pre-existing Aitken mode particles and background aerosol loading, making it difficult to isolate NPF signals at larger sizes. Horizontal dashed lines indicate the diameter ranges selected for subsequent analysis (3–12 nm for total particles and 2–4 nm for ions). These demarcated windows capture the size range where NPF signatures are most reliably observed and help refine the diameter thresholds used in standard NPF classification approaches.

Building on the size–time evolution shown in Fig. 2, the monthly statistical distributions of number concentrations within the selected diameter ranges are presented in Fig. 3. The figure shows total particles (7–12 nm and 3–5 nm) and ions (2–4 nm) as paired daytime and nighttime violin plots representing kernel density estimates. Within each violin, a box plot indicates the monthly median (central line), interquartile range (box), and 5–95 % percentiles (whiskers) for daytime (6–18 h LT) and nighttime (18–6 h LT) concentrations. Within the retained 3–12 nm range identified in Fig. 2, Fig. 3 presents two narrower sub-windows, 3–5 nm and 7–12 nm. The 3–5 nm window isolates particles closest to the NAIS lower detection limit, capturing the earliest stage of a growing mode while limiting

the contribution of larger, locally influenced particles, including traffic emissions, that increasingly populate the distribution above about 5 nm in this urban-influenced setting.

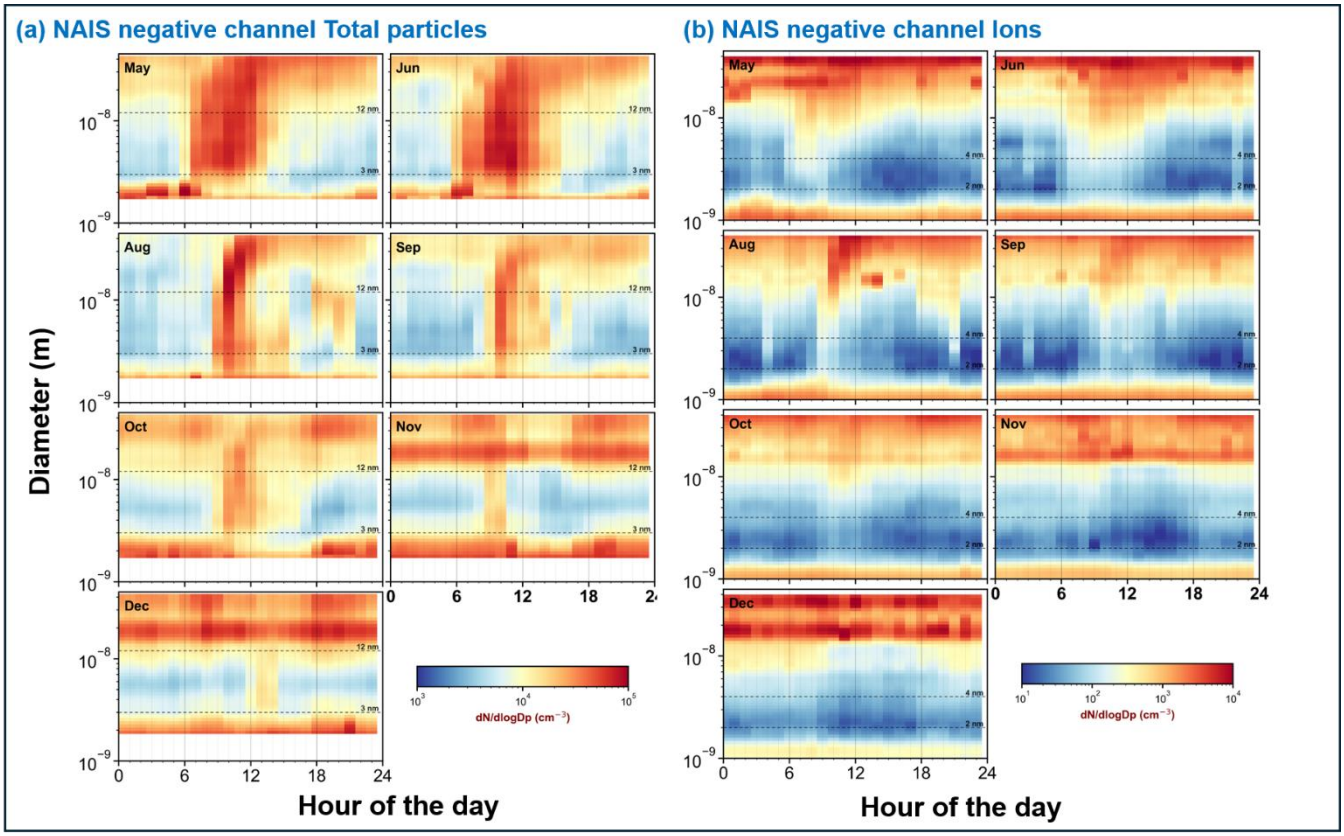

Figure 2: Heatmap showing size-resolved monthly mean variations of (a) particle-mode PNSD (ions + neutral particles) and (b) ions PNSD for May, June, August, September, October, November, and December 2023 at CAS-AO. Horizontal dashed lines indicate the diameter bins used in further analysis (2 and 4 nm for ions; 3 and 12 nm for particles).

The 7–12 nm window remains conservatively below the approximately 12 nm threshold beyond which background Aitken-mode aerosol dominates the signal, as established in Fig. 2. Across the 7–12 nm size range in Fig. 3(a), particle concentrations show a seasonal and diurnal contrast. During summer (May–June), daytime median concentrations reach on the order of 3–5 × 10^3 cm^{-3}, approximately two to three times higher than nighttime levels (~1–2 × 10^3 cm^{-3}). The distributions are also substantially broader during the day, with upper percentiles extending well above 8 × 10^3 cm^{-3}, indicating episodic but intense production events rather than uniform background enhancement. In contrast, August and September exhibit more moderate daytime increases (median ~1–2 × 10^3 cm^{-3}) with reduced day–night contrast, while October–December show comparatively compact distributions and, in some cases (November–December), slightly higher nighttime medians, suggesting suppressed NPF and a stronger influence of background accumulation.

A similar pattern is observed for the 3–5 nm size range in Fig. 3(b), which represents freshly formed particles (relatively). In May and June, daytime medians approach ~3×10^3 cm^{-3} and exceed nighttime values by a factor of ~3–3.5, consistent with frequent and strong NPF activity. The enhancement weakens progressively toward late monsoon and post-monsoon months, with September and October showing only marginal day–night differences (~1.0–1.1 ratio). By November and December, nighttime concentrations become comparable to or slightly higher than daytime levels, reflecting the absence of sustained nucleation bursts and more stable aerosol conditions. In contrast, ion concentrations in the 2–4 nm range in Fig. 3(c) remain much lower in absolute magnitude (generally 5–12 cm^{-3}), with moderate daytime enhancement during May–August (day/night ratios ~1.5–2.5). However, unlike particles, ions display weaker seasonal variability and in late autumn–winter (October–December) occasionally exhibit higher nighttime medians, suggesting that ion abundance alone does not scale directly with the intensity of particle growth. Together, these distributional analyses quantitatively confirm the seasonal and diurnal patterns inferred from the heatmaps: strong and sustained daytime particle production during warmer months, a gradual weakening through the monsoon transition, and comparatively stable, background-dominated conditions in winter.

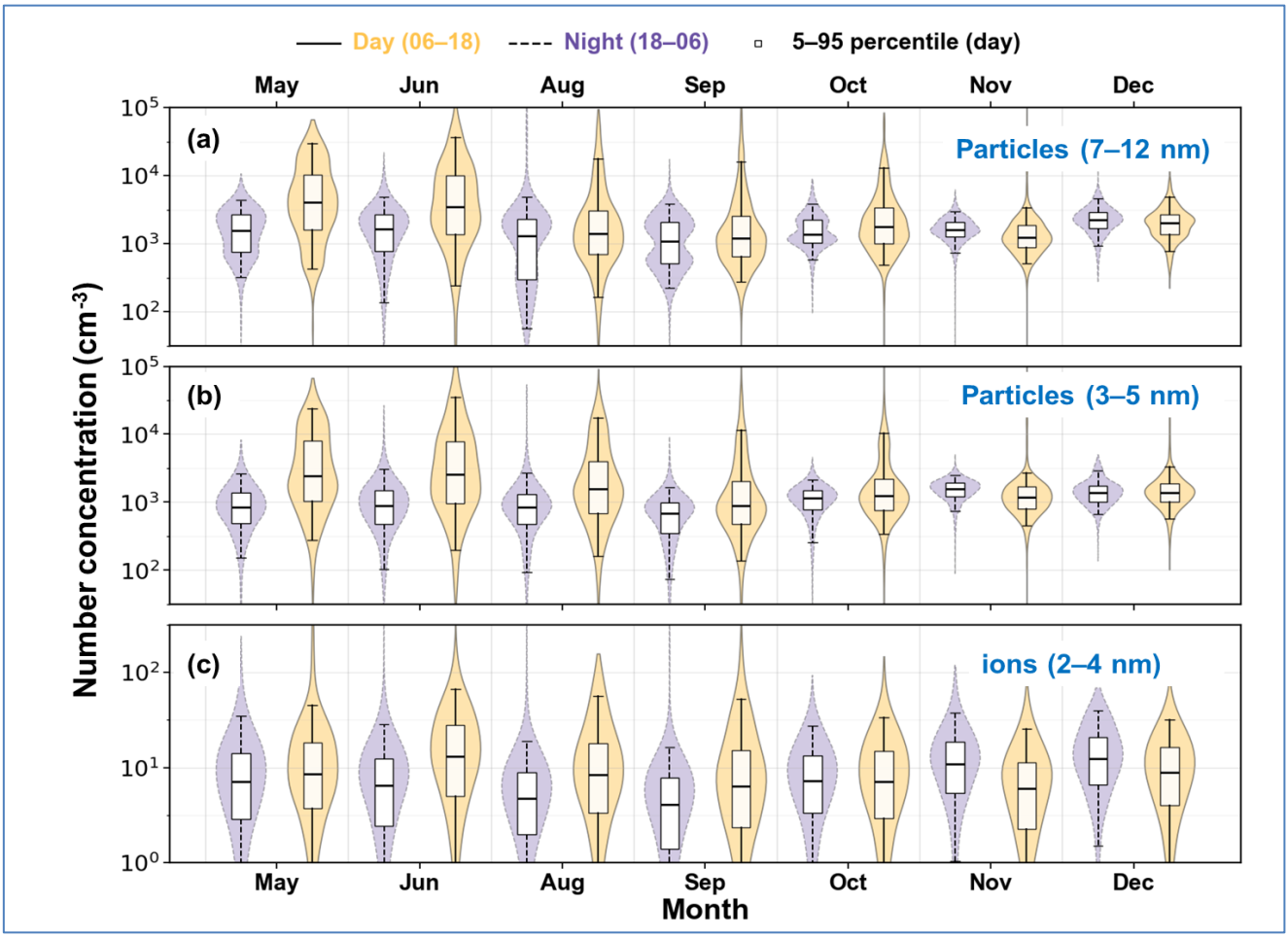

Figure 3: Monthly distributions of daytime (6–18 h LT) and nighttime (18–6 h LT) number concentrations, during May–December 2023, for (a) particles in the 7–12 nm size range, (b) particles in the 3–5 nm size range, and (c) ions in the 2–4 nm size range. Violin plots illustrate the full probability distribution of concentrations, while embedded box elements indicate the monthly median (central line), interquartile range (box), and 5–95 % percentiles (whiskers) of daytime (6–18 h LT) and nighttime (18–6 h LT) number concentrations. Daytime and nighttime periods are distinguished by solid and dashed outlines, respectively.

3.2 New particle formation at a suburban site upwind of Delhi

New particle formation (NPF) events were identified across the observational period (May–December 2023) at CAS-AO, Sonipat, representing a suburban site located approximately 50 km upwind of Delhi in the IGP (Rathore et al., 2025). The site experiences substantial seasonal variability in meteorological conditions and aerosol loading (Section 3.1), both of which modulate the frequency and intensity of NPF. Given that the IGP is characterised by elevated background aerosol concentrations and high condensation sinks, the detection and classification of NPF events is non-trivial and depends significantly on the choice of methodology. To address this, we applied three complementary classification frameworks of increasing complexity and objectivity, as described in the methodology section, and the results are presented below.

3.2.1 NPF event classification using different frameworks

Using the Dal Maso et al. (2005) method, we identify a total of 10 Class I events (9 % of valid NAIS days), 40 Class II events (37 % of valid NAIS days), and the remaining 58 non-event days (54 % of valid NAIS days) over the 108-day study period. A seasonal modulation in NPF occurrence is evident. During May and June, the majority of days fall into Class I or Class II (11 out of 12 in May and 19 out of 23 in June), indicating frequent and well-developed particle formation. The corresponding absolute monthly Dal Maso class counts are provided in Fig. S3.

To complement this traditional visual classification and to reduce subjectivity, we further applied an automated event detection approach proposed by (Dada et al., 2018). This framework combines ion and particle number concentrations (7–25 nm size range for particles and 2–4 nm ion concentrations). This enables a more process-based distinction between local particle formation, transported event signatures, and ion burst events based on the concurrent behaviour of cluster-sized ions and larger particles. As detailed in methodology section, we restricted the elevated particle concentration criterion to 7–12 nm to account for site-specific noise characteristics. Using this methodology, warmer months (May–June) show the highest occurrence of regional NPF events (66 % and 86 % of total available days respectively). This indicates favourable conditions for local particle formation and growth. August, September and October have relatively fewer combined regional and transported event-days. Winter months (November, December) predominantly experience non-event days (88 % and 87 % respectively). Ion Bursts are relatively rare throughout the year, and none were observed in our dataset.

Results are summarised in Fig. 4, which presents the monthly distribution of event categories from both classification schemes as stacked bar charts normalised to highlight seasonal contrasts. The stacked bar chart from this scheme demonstrates distinct seasonal patterns in NPF event occurrences. This seasonal transition may be attributed to favourable photochemical and dynamical conditions for nucleation during the warmer months. Winter conditions appear less conducive to sustained particle formation and growth. This can be possibly associated with reduced photochemical activity, effect of low wind speeds, usually high-pressure zone persistence and shallower boundary layer height typically observed during winter at this site.

Comparing the two schemes directly (Fig. 4), there is broad seasonal agreement: both identify May and June as the most active months and November–December as predominantly non-event. However, the Dada et al. (2018) classification consistently assigns a higher fraction of days to active categories than Dal Maso et al. (2005). For example, in August, Dal Maso identifies 50 % non-events whereas Dada assigns 60 % of days as regional or transported Events. This divergence is expected, as the Dada framework captures transported and partially

developed events that the visual scheme places in Class II or non-event. The fraction of transported events (TE) is notably elevated in August–October, suggesting advection of particles or precursors rather than local formation during this transitional period. The corresponding absolute Dada class counts are provided in Fig. S4.

Dada et al. (2018) can be regarded as an updated extension of the Dal Maso et al. (2005) classification, with consideration on lower size-range number concentrations and ion contribution to NPF events. This approach allows ion burst events and transported events to come into the picture. However, the distinction between regional and transported events is often subtle. The occurrence of transported Events suggests that particles formed in surrounding regions are being advected to the CAS-AO site. Usually, the days with high winds can efficiently transport the precursors as well as some fraction of particles. It is also possible that some transported Event classifications reflect anthropogenic emission signatures in the sub–12 nm size range rather than true NPF advection. Ion signals in the lower size range can be masked by external influences such as enhanced condensation sinks, local emissions, or meteorological conditions, which may obscure their detection by the instrument.

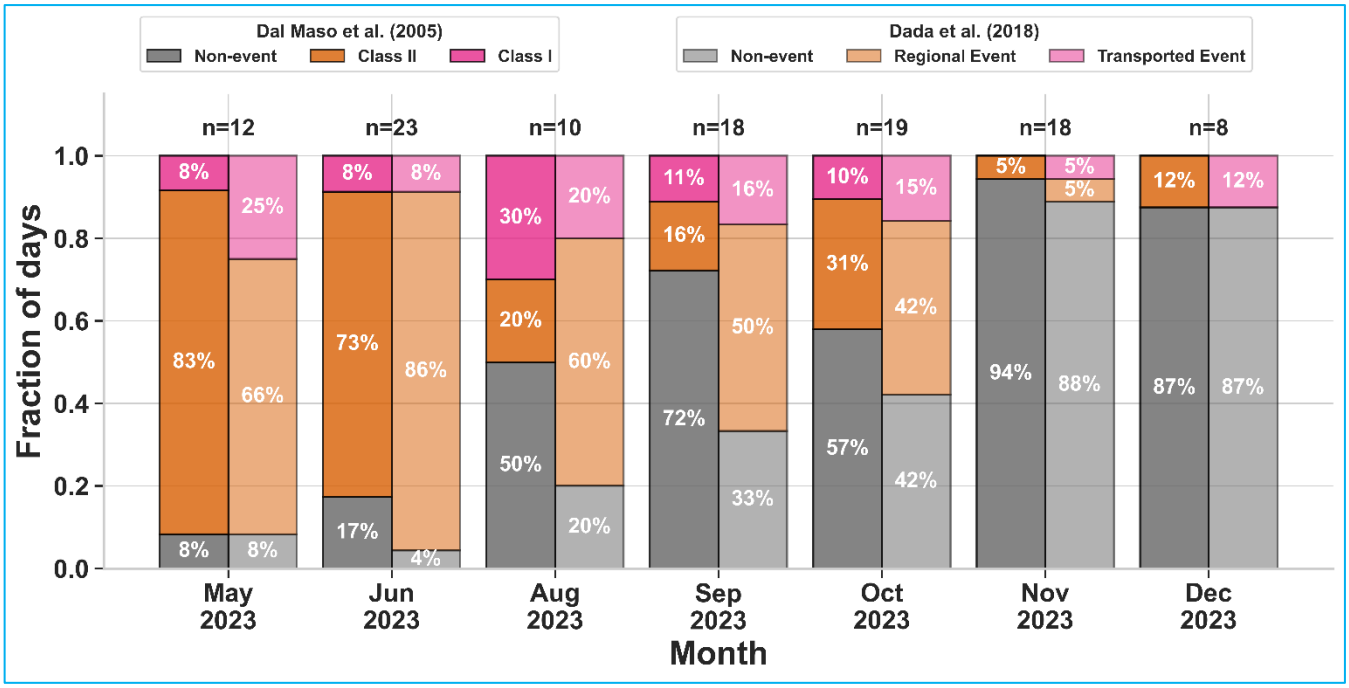

Figure 4: Monthly fraction of days at CAS-AO (May-December 2023) classified following the modified scheme of Dal Maso et al. (2005) left bars and Dada et al (2018) right bars. Days are categorised as Non-event, Class II, and Class I (for Dal Maso et al. 2005) and non-event, regional event, and transport event (for Dada et al. 2018). Numbers inside bars are percentage of days with total number of days in each category for each month, and at top of each bar "n" denotes the total number of days per month.

To make the classification picture clearer, we next applied the scheme proposed by Aliaga et al. (2023). Fig. 5 presents the median diurnal PNSD for each 5 % percentile group using Aliaga et al. (2023). The heatmaps span diameters from approximately 2–42 nm, enabling visualisation of both nucleation-mode particles and their subsequent growth. Guiding horizontal lines at 3 and 5 nm are drawn to indicate the size range used for the ΔN ranking parameter. A systematic transition in NPF intensity is evident across the percentile ranks. The lowest percentile groups (0–40 %) show very weak or negligible formation activity, with relatively stable concentrations across sizes. Intermediate groups (40–65 %) begin to exhibit modest enhancement, suggesting partial or weak NPF activity. The highest percentile intervals (65–100 %) display clear burst and growth patterns initiating in the morning hours and extending toward larger diameters later in the day, indicative of sustained new particle formation and growth.

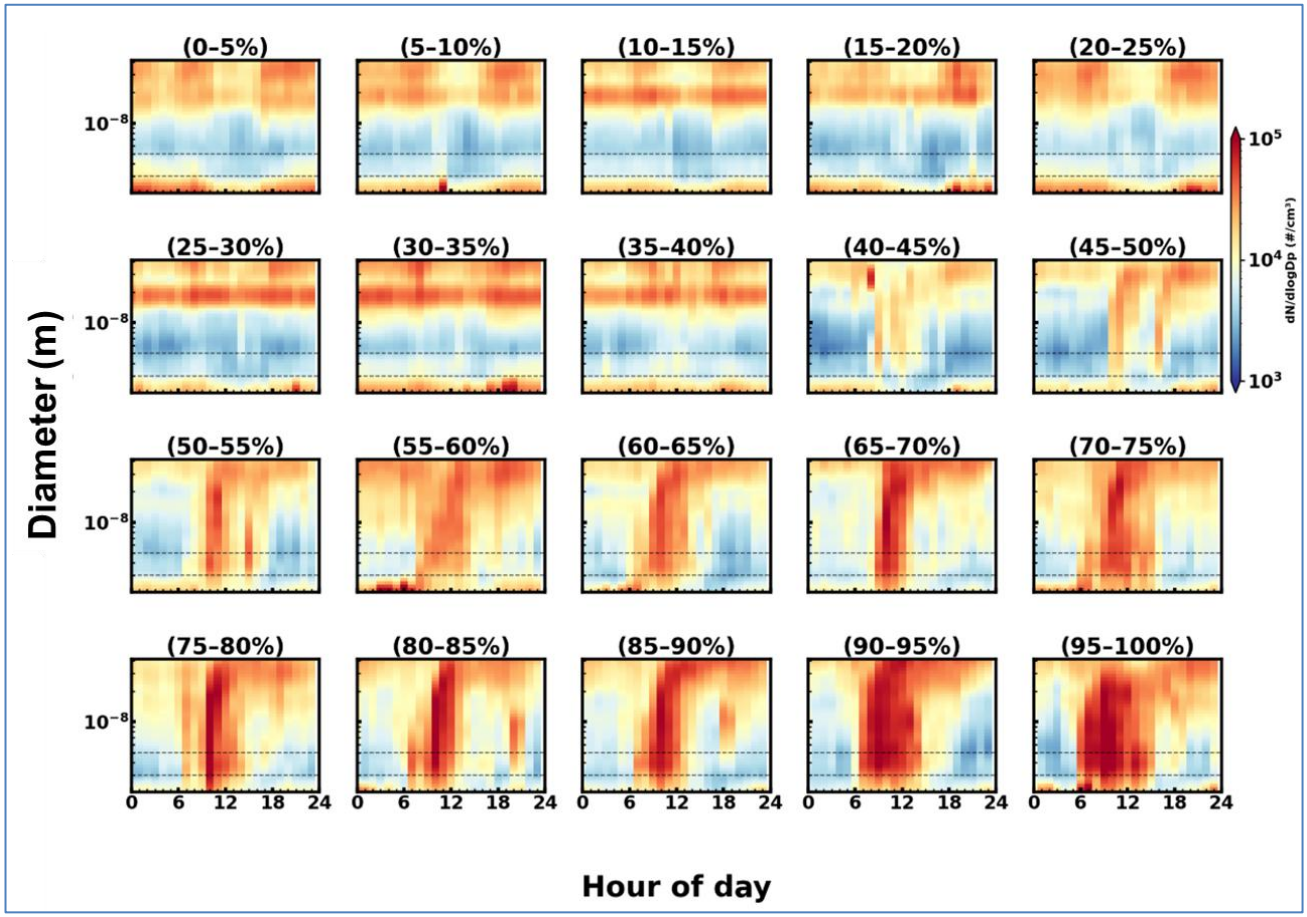

Figure 5: Daily median particle number size distributions grouped in 5 % intervals based on $\Delta N_{2.5-5}$ ranks. Each panel shows the diurnal evolution of particle number size distributions for a specific percentile interval., with colour indicating particle number concentration (cm^{-3}). Horizontal guiding lines are drawn at 3 nm and 5 nm to help in visualizing the ranking parameter.

Fig. 6 presents a comprehensive analysis of NPF events using Aliaga et al. (2023)'s percentile ranking approach overlaid with event classification from Dada et al. (2018). NPF events identified by Dada et al. (2018) (regional and transported Events) cluster predominantly in the higher percentile groups (60–100 %), with very few events in percentiles below the 30th percentile. Within the high-percentile groups, May and June contribute the largest fraction of events, consistent with the seasonal patterns identified in both preceding classification schemes.

The combined application of the classification approach of Dada et al. (2018), rooted in the framework of Dal Maso et al. (2005), and the nanoparticle ranking analysis of Aliaga et al. (2023) offers complementary perspectives on NPF. The Dada et al. 2018 methodology focuses on the temporal evolution of ion and PNSD within individual days, categorising events according to their developmental characteristics (e.g. regional formation, transported influence, or weaker ion-related activity), and thereby emphasises process-level interpretation based on daily growth signatures. In contrast, the Aliaga et al. (2023) ranking method evaluates NPF intensity using a statistical metric derived from longer-term variability in a selected size range (3–5 nm in this study) placing each day within a broader context of event strength over the full data set.

When applied together, the two approaches show general consistency. Days categorised as clear formation events in the Dada et al. (2018) framework tend to fall within the higher ΔN percentiles in the ranking analysis. At the same time, the agreement is not exact for some days, which is expected given the different conceptual bases of the methods. The Dada classification may identify transported bursts based on their temporal development, whereas the percentile-based approach quantifies the magnitude of concentration enhancement without explicitly distinguishing its physical origin. In both cases, possibly local anthropogenic sources, particularly traffic emissions given the site's suburban location upwind of Delhi, may influence the elevated particle concentrations whether from regional NPF, transported growth, and so the classification outcome. Therefore, neither framework alone can fully resolve the underlying mechanisms without additional supporting analyses.

Class-composite mean and median PNSD for the classification schemes are provided in Fig. S5. Each of the three classification frameworks carries inherent limitations that are particularly relevant in the suburban context of CAS-AO. The Dal Maso et al. (2005) method, despite its physical intuition, depends on manual visual inspection, introducing observer subjectivity and limiting reproducibility; the high fraction of Class II events in this dataset (37 %) reflects the difficulty of unambiguously resolving nucleation modes against the elevated background aerosol typical of an environment downwind of a megacity. The Dada et al. (2018) method reduces this subjectivity through automation, but its reliance on 2–4 nm ion signals make it vulnerable to masking by the high condensation sinks and anthropogenic aerosol loading characteristic of this site. The Aliaga et al. (2023) ranking approach avoids categorical ambiguity by assigning a continuous intensity metric to every day, but ΔN_{3-5} is not source-specific: elevated sub–5 nm concentrations can arise from traffic emissions or other primary sources rather than NPF, a concern that is amplified at a site located upwind of Delhi where anthropogenic precursor and primary particle loads are substantial. All three methods are additionally sensitive to the pre-existing aerosol loading, a high condensation sink suppresses the observable nucleation signal regardless of the actual nucleation rate, meaning that genuine NPF events may be systematically underestimated or misclassified under the polluted conditions frequently encountered at this site. These limitations reinforce that the three methods should be treated as complementary rather than independently sufficient diagnostics, and that confident mechanistic attribution requires supporting data on precursor gas concentrations, air mass origin, and boundary layer dynamics.

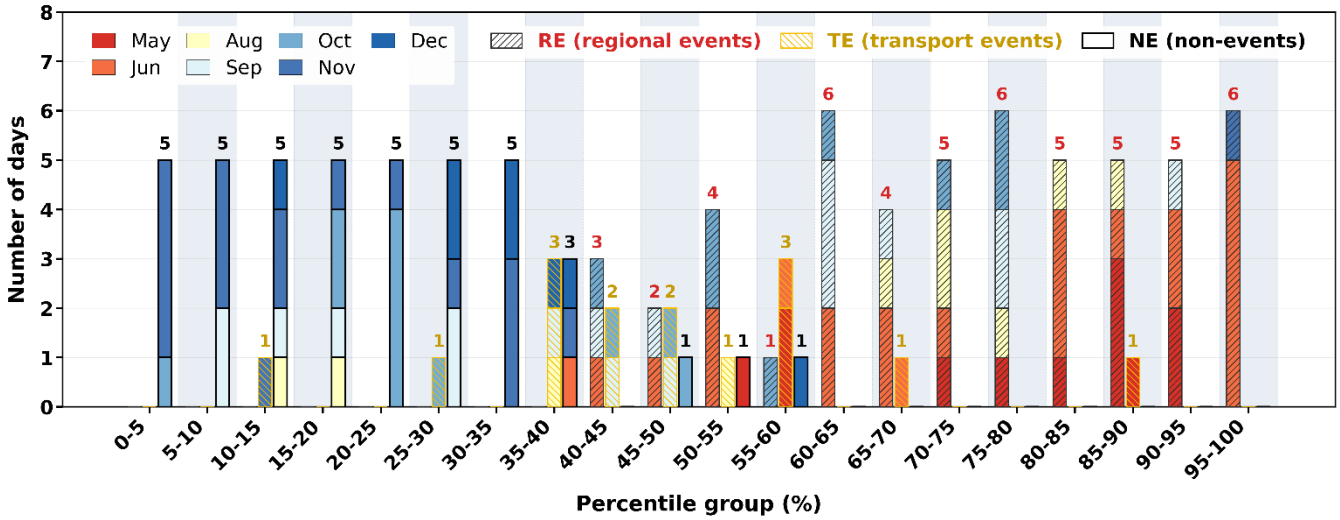

Figure 6: Seasonal distribution of Dada et al. (2018) event categories, grouped by $\Delta N_{2.5-5}$ percentile intervals. The x-axis displays percentile groups based on ΔN_{3-5} particle concentration rankings (from 0–5 % to 90–95 %), while the y-axis shows the number of events. Each bar is color-coded by month and differentiated by pattern for regional events (forward hatched), transported events (backwards hatched) and non-events (solid). Total event-days observed in the analysis period for each percentile are marked at top of the bars.

3.2.2 NPF parameters: growth rates, condensation sink and formation rates

Figure 7 presents the distribution of particle growth rates (GR) for size ranges 3-7 nm and 7-20 nm, derived using the Gaussian/mode-peak and appearance-time methods. For the nominal 3-7 nm range, the appearance-time method yielded 6 successful fits with a median GR of 10.6 nm h^{-1} and IQR of 7.9-15.9 nm h^{-1}, while the Gaussian/mode-peak method yielded 5 successful fits with a median GR of 14.7 nm h-1 and IQR of 10.2-18.0 nm h^{-1}. For the nominal 7-20 nm range, the appearance-time method yielded 12 successful fits with a median GR of 16.8 nm h^{-1} and IQR of 13.9-26.6 nm h^{-1}, while the Gaussian/mode-peak method yielded 15 successful fits with a median GR of 19.0 nm h^{-1} and IQR of 16.4-20.4 nm h^{-1}.

The growth rate values should be interpreted as fitted values within the nominal 3-7 nm and 7-20 nm ranges rather than unconditional full-window averages. In several cases, only a contiguous sub-range could be fitted because parts of the nominal interval were affected by weak mode separation, plume-like variability, or missing data. The contiguous sub-ranges were chosen by visual inspection so that the change in appearance or maximum-concentration times across NAIS channels followed the investigated growing mode without being heavily affected by these variabilities. Most commonly, the fitted feature was affected either by the mode appearing or disappearing abruptly across a wide diameter range while otherwise growing steadily, or by high-concentration plumes during the event, which made the maximum concentration of the growing mode and its occurrence time impossible to determine reliably from channel-wise fitting.

The measurement period included episodic pollution plumes in which particle number concentrations occasionally rose abruptly or produced enhancements comparable in magnitude and timing to NPF growth signals. Wind-driven variability further introduced choppiness in size-bin time series. Growth rates reported here were derived after

careful manual screening to minimise such contamination, and event-wise diagnostic heatmaps are presented in supplementary Fig. S6. However, residual influence cannot be entirely excluded. Event-wise fitting diagnostics for the retained GR cases are provided in Fig. S7, showing the fitted appearance-time and Gaussian/mode-peak points used in the GR calculations together with the corresponding PNSD.

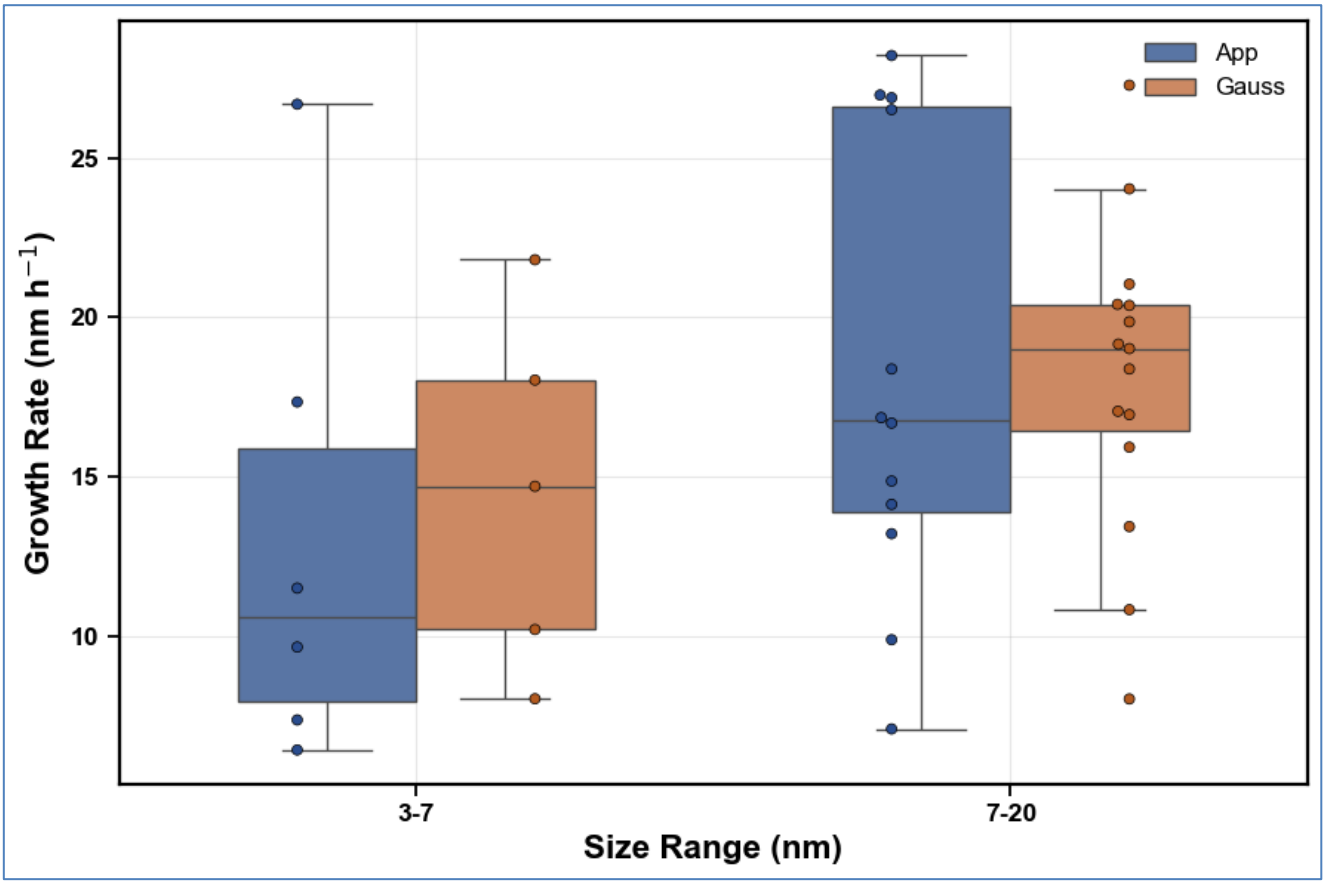

Figure 7: Distribution of particle growth rates (GR) in size ranges 3–7 and 7–20 nm derived using the Maximum concentration method (using Gaussian fitting) and appearance time methods (using sigmoid function). Boxplots show the median and interquartile range, with whiskers representing the range excluding outliers. Individual markers denote event-wise GR values.

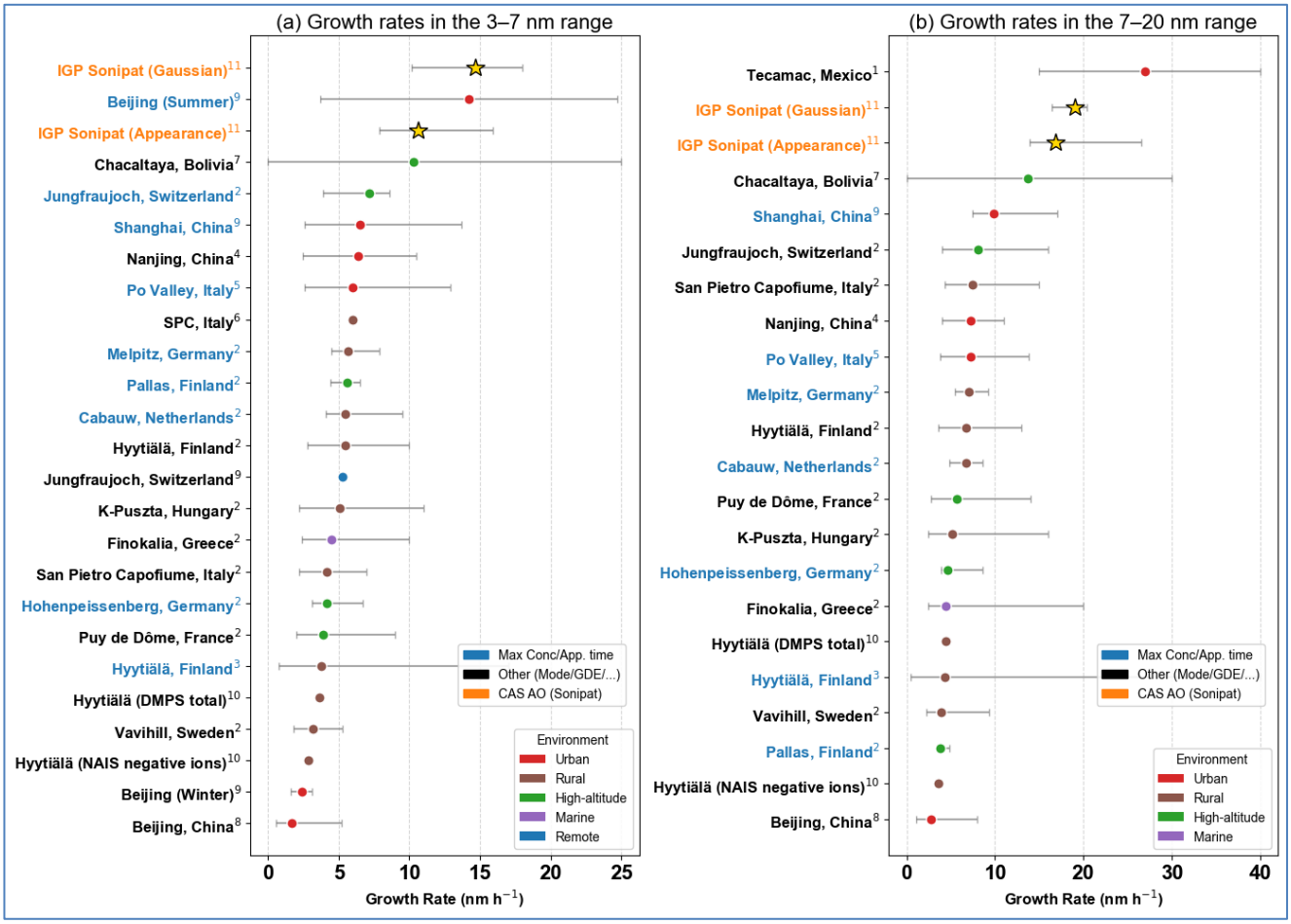

Figure 8: Global comparison of particle growth rates (GR) in the (a) 3–7 nm and (b) 7–20 nm size ranges across diverse atmospheric environments. Circles represent reported median GR values from literature studies, with horizontal whiskers indicating the reported variability range (min–max where available). Colours denote environment type (high-altitude/background, marine/coastal, rural, and urban). Star symbols highlight values from the present study conducted in the (CAS-AO) Indo-Gangetic Plain (IGP), Sonipat, derived using Gaussian peak fitting and appearance time methods. Growth rates are expressed in nm h^{-1}. Entries with slightly different upper size bounds (e.g., 7–15 nm or 7–25 nm) are included in the 7–20 nm panel for comparison and are noted in the corresponding references. (1: Iida 2008; 2: Manninen 2010; 3: Yli-Juuti 2011; 4: Herrmann et al., 2014; 5: Kontkanen 2016; 6: Kulmala 2017; 7: Sellegri 2019; 8: Yu 2020; 9: Stolzenburg et al., 2023; 10: Lampilahti 2025; 11: This Study).

Figure 8 presents a global comparison of particle GR in the 3–7 nm and 7–20 nm size ranges across diverse atmospheric environments, including remote, high-altitude/background, marine/coastal, rural, polluted regional, and urban locations. Literature-reported median GR values are compiled from long-term and multi-site analyses e.g., (Iida et al., 2008; Manninen et al., 2010; Yli-Juuti et al., 2011; Herrmann et al., 2014; Kontkanen et al., 2016; Kulmala et al., 2017; Kerminen et al., 2018; Sellegri et al., 2019; Yu et al., 2020; Stolzenburg et al., 2023; Lampilahti et al., 2025) and are shown as circles with horizontal whiskers indicating the reported variability range

(min–max where available). The values from the present study conducted in the IGP, Sonipat CAS-AO, derived using max conc. and appearance time methods, are highlighted with star symbols. For consistency, entries with closely matching upper bounds (e.g., 7–15 nm or 7–25 nm) are included in the 7–20 nm panel for comparative purposes. In the 3–7 nm size range, the GR values from the present study fall within the upper range of urban and polluted regional environments, exceeding most background and remote site values. In the 7–20 nm range, the max conc. derived values remain closer to the central tendency of urban literature reports, whereas the appearance time method highlights episodes of enhanced growth that shift the site toward the upper envelope of reported values. The comparison suggests that the particle growth in the IGP is elevated compared to cleaner environments, particularly at larger particle sizes consistent with elevated condensable vapour concentrates expected in the anthropogenically influenced IGP boundary layer.

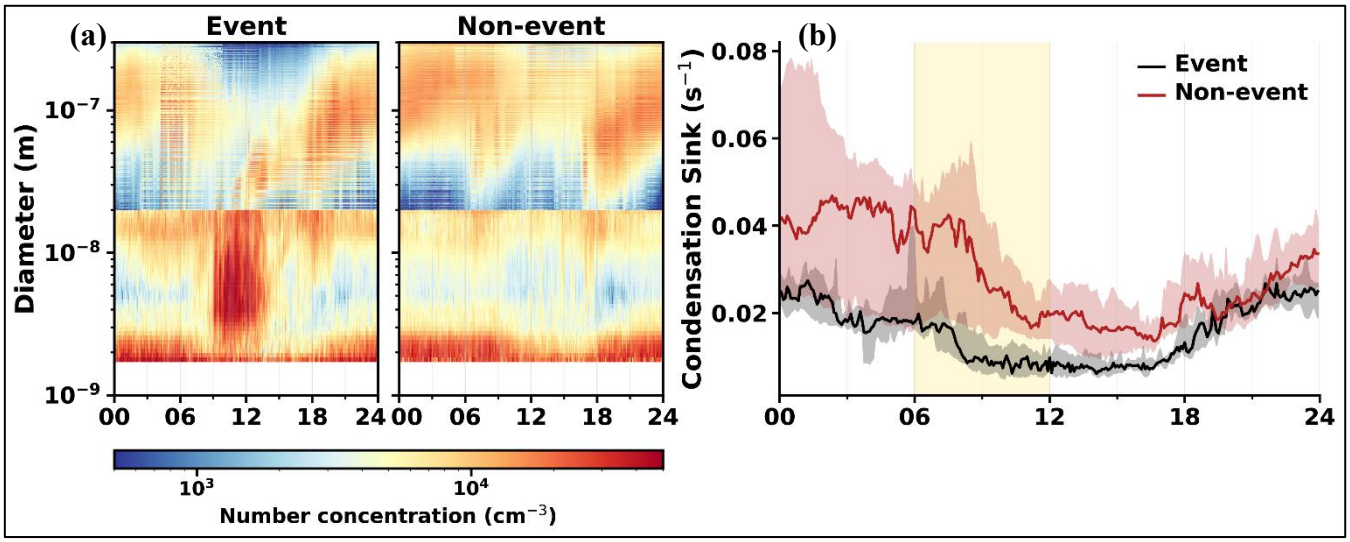

Figure 9: (a) Diurnal composite aerosol particle number size distributions and (b) condensation sink during new particle formation (NPF) event and non-event days. Left panel (a) shows the median particle number size distribution as a function of time of day for event-days (left) and non-event days (right), combining NAIS (sub–20 nm) and SMPS (>20 nm) measurements. The colour scale represents particle number concentration (cm^{-3}), and the y-axis is shown in logarithmic diameter scale. The right panel (b) shows the diurnal variation of the condensation sink (CS) for event-days (black) and non-event days (red), with shaded regions indicating the interquartile range (25–75 %). The shaded vertical band highlights the typical nucleation time window (6–12 h LT).

Figure 9(a) presents the composite diurnal behaviour of PNSD and Fig. 9(b) presents the condensation sink for event and non-event days. Because comparison of CS between event and non-event days requires the combined NAIS-SMPS PNSD, Fig. 9 is based only on the concurrent-instrument subset (9 event days and 15 non-event days). The left panels show median PNSD as a function of time of day for event and non-event days. For this 06:00-12:00 LT window, the event-day median CS was 0.0095 s^{-1} (IQR: 0.0074-0.0147 s^{-1}; n = 9), compared with 0.0292 s^{-1} (IQR: 0.0171-0.0413 s^{-1}; n = 15) on non-event days.

During the typical nucleation window (~6-12 h LT), event days consistently maintain lower CS values, particularly during late morning to early afternoon, when particle formation and growth are most active. The reduced CS during

these periods implies a weaker scavenging environment, allowing newly formed clusters to grow to detectable sizes. Previous observations in Delhi show that NPF events are typically observed when CS remains below ~0.06 s^{-1}, despite a wider observed CS range, indicating that sufficiently reduced sink conditions are needed for particle formation and sustained growth (Ali et al., 2025). Studies in Beijing have also found that NPF events typically occur when CS remains below ~0.03 s^{-1}, while higher values suppress cluster survival (Deng et al., 2021). In contrast, much lower condensation sinks (~10^{-3}-10^{-2} s^{-1}) are typical of cleaner environments such as boreal forest sites, highlighting the strong influence of background aerosol loading on NPF occurrence across atmospheric regimes.

Studying NPF in polluted environments presents substantially greater challenges compared to relatively clean conditions. In our measurements, several days exhibited visually identifiable NPF-like signatures; however, these were frequently obscured by irregular and non-systematic contributions from multiple emission sources. These sources introduced additional modes in the PNSD, often overlapping with or masking the growing nucleation mode. In some cases, the pollution-related modes dominated the signal, completely suppressing the visibility of NPF, whereas in other cases, the growth appeared only as a shoulder adjacent to a broader pollution plume. In such environments, traditional manual approaches relying on visual inspection become less reliable, and fully automated methods often fail to capture the complexity of the data.

Further complications arise from instrumental noise and meteorological variability. Wind fluctuations and precipitation intermittently dilute or distort the particle concentrations, leading to fragmented or discontinuous signatures. While rainfall is less frequent during summer and winter, elevated wind speeds during these periods can still significantly perturb the observed distributions. Together, these factors introduce substantial variability that complicates the identification and interpretation of NPF events.

The classification of NPF events under such conditions inherently carries uncertainty. The widely used visual framework like Dal Maso et al. (2005) classification scheme relies on visual interpretation and investigator judgment. Variations in color scale, plotting choices, and subjective interpretation can lead to inconsistencies. While such discrepancies are minimal in cleaner environments, polluted conditions introduce substantial ambiguity, resulting in lower inter- and intra-observer agreement. Semi-automated and automated approaches, such as those proposed by Dada et al. (2018) method and Aliaga et al. (2023) method, offer promising alternatives. However, these methods typically rely on detectable enhancements in particle number concentrations within specific size ranges. In polluted environments, such enhancements are often masked, fragmented, or confounded by overlapping sources, limiting the effectiveness of these techniques. Consequently, careful day-by-day inspection remains necessary to identify genuine NPF signals.

Despite these methodological challenges, consistent patterns emerge from the combined classification and concentration analyses, providing insight into the processes governing NPF at this site. All methods indicate that summer is more conducive to NPF events, whereas winter periods are generally less favourable for sustained particle formation. This seasonal variability is apparent in particle number concentration, but ion concentrations show weaker seasonal variability. This suggests that ion availability is not the primary constraint on particle formation in this region. The observed decoupling between ion and nucleation-mode particle dynamics indicates that precursor vapour abundance and the condensation sink play more important roles in controlling particle

survival and growth. This interpretation is further supported by the presence of transported events and the absence of clear ion bursts in some particle-growth cases. Further chemical characterisation of precursor vapours would be required to confirm these pathways.

The estimation of particle GR is similarly affected. Most existing studies e.g., (Kulmala et al., 2012; Lehtipalo et al., 2014; Paasonen et al., 2018) focus on relatively clean conditions characterised by distinct lognormal modes. In contrast, our dataset frequently exhibits multiple overlapping modes with varying intensities, requiring manual intervention in the fitting process. Due to these non-ideal conditions, it is not always possible to estimate GR over a consistent size range across all days. In several cases, the growing mode is only weakly visible or appears as a shoulder of a dominant pollution-related mode.

Fig. 10 shows two representative days influenced by pollution-source spikes. In the left panel, the NPF-related particle-number increase is stronger and more continuous than the pollution spikes, so a growth rate could be calculated. In the right panel, nucleation and partial growth signatures are visible, but wind shifts and pollution spikes distort the size distribution, and a reliable growth rate could not be obtained.

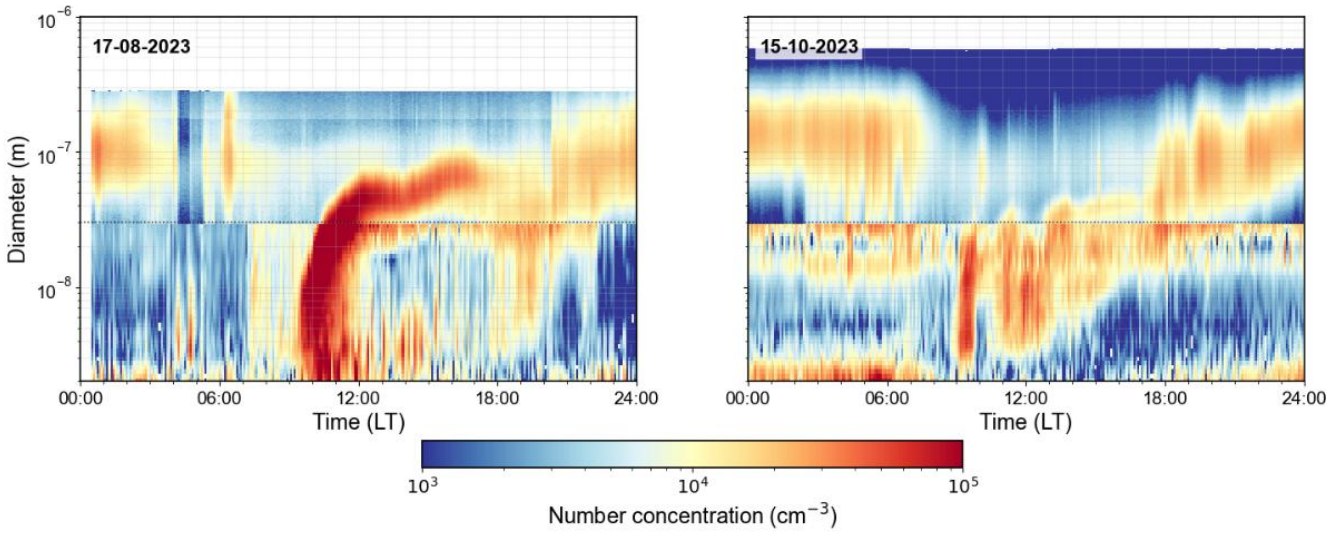

Figure 10: Time–diameter evolution of particle number size distributions for selected days (17 August and 15 October 2023) at CAS-AO, obtained from merged NAIS (≤ 30 nm) and SMPS (> 30 nm) measurements. The colour scale represents particle number concentration (cm^{-3}) on a logarithmic scale.

Table 1: Particle formation rates at 3 nm (J_3) and 7 nm (J_7), growth rates, and condensation sink for NPF days at CAS-AO. Growth rates ($GR_{3–7}$ and $GR_{7–20}$) are derived for the 3–7 nm and 7–20 nm size ranges, respectively. For the J_7 the growth rate has been calculated for the sub size range between 7 and 20 nm accordingly where it was reliably possible to calculate it. For the J_7, particle number concentration between 7 to 12 nm is used to avoid instrument artifact and possible other emission sources.

Date	J_3 ($cm^{-3}s^{-1}$)	J_7 ($cm^{-3}s^{-1}$)	GR_{3_7} (nmh^{-1})	GR_{7_20} (nmh^{-1})	CS (s^{-1})
17-08-2023	-	50.0	-	27.3	0.0120
18-08-2023	80.8	53.5	26.7	19.0	0.0095
07-10-2023	-	59.2	-	15.9	0.0093

3.3 Role of condensation sink and meteorological conditions on NPF occurrence:

During the post-monsoon and winter transition period over the Indo-Gangetic Plain, aerosol loadings are typically elevated and dominated by accumulation-mode particles, leading to enhanced condensation and coagulation sinks. Consequently, clear and sustained NPF events are generally less frequent during this season which has been demonstrated by the classification results in section 3.2. Nevertheless, intermittent NPF events are occasionally observed under favourable combinations of reduced sink strength and supportive meteorological conditions. To illustrate the processes enabling NPF under such otherwise unfavourable background conditions, we examine in detail the period from 5–10 October 2023, which includes a well-defined NPF event on 7 October 2023.

Figure 11 illustrates the time-diameter evolution of particle number concentrations and sink parameters during 5–10 October 2023, encompassing both NPF and non-event days. The figure combines size-resolved measurements from (a) SMPS, (b) NAIS negative-ion channel, and the corresponding (c) condensation sinks. The SMPS and NAIS spectrograms illustrate the temporal evolution of particle populations across the nucleation, Aitken, and accumulation modes. Dashed horizontal lines mark reference diameters at 2 and 25 nm. All panels share a common time axis, enabling direct comparison between PNSD and sink dynamics over the same period.

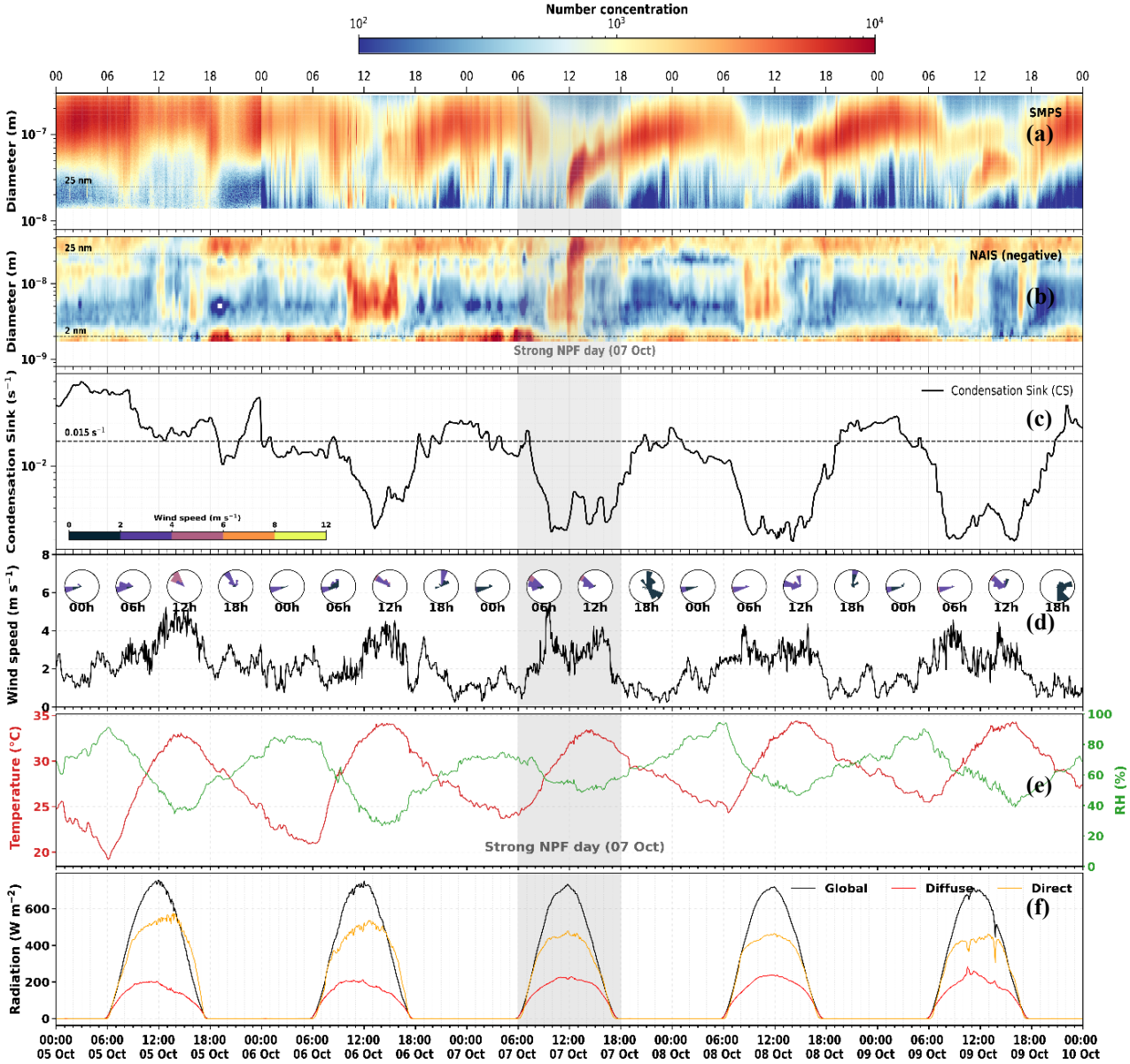

Figure 11: Time series of different variables during NPF observation period (5–10 October 2023). (a) Time–diameter spectrograms of particle number concentration measured by SMPS (b) NAIS negative channel particle number size distribution (c) condensation sink (CS) with the dashed horizontal line indicating the CS = 0.015 s^{-1} for reference. (d) Wind speed during the period with wind direction shown as wind roses for each 6 hours (e) air temperature & relative humidity (f) global, diffuse, & direct solar radiation measured at the CAS-AO. The shaded region highlights the NPF event-day (7 October 2023). For (a) and (b) the colour indicates number concentration (cm^{-3}) on a logarithmic scale. Horizontal dashed lines mark 2 nm and 25 nm particle diameters.

Figure 11 (d), (e) and (f) summarises the synoptic and local meteorological conditions during the same period encompassing the NPF event on 7 October 2023. Wind speeds exhibit moderate variability throughout the period, with the event-day characterised by predominantly north-westerly flow and moderate wind speeds, conditions associated with enhanced ventilation and lower background aerosol accumulation. Wind direction shows intermittent variability on non-event days, suggesting changing air mass influences that may contribute to fluctuating aerosol loadings. Concurrent low relative humidity (~35 %) and elevated temperature (~30 °C) on 7 October 2023 further support favourable nucleation conditions. Similar meteorological features may also occur on non-event days; however, NPF occurrence reflects the combined influence of favourable meteorology, precursor availability, and sufficiently reduced sink conditions, no single factor being independently sufficient. On 7 October, the daily median CS was 0.0158 s^{-1} (IQR: 0.0078-0.0199 s^{-1}), and during 06:00-12:00 LT it was 0.0093 s^{-1} (IQR: 0.0056-0.0185 s^{-1}). Thus, the event occurred during a low-CS morning period relative to surrounding polluted conditions.

The combined PNSD from NAIS and SMPS, together with sink parameters, show a temporal correspondence between particle population dynamics and sink strength. Periods with enhanced nucleation-mode particle number concentrations in the NAIS spectrogram consistently coincide with reduced CS values. In contrast, days with persistently elevated sink values show no corresponding clear event-specific growth features in the nucleation-mode range, indicating conditions unfavourable for particle formation and early growth.

To place observations from the CAS-AO in a broader urban pollution context, the CS values obtained in this study are interpreted alongside reported environmental ranges and process-based thresholds governing NPF. As established in Section 3.2, event-day CS values during 06:00-12:00 LT (~0.0095 s^{-1}) were lower than non-event values (~0.0292 s^{-1}), indicating a reduction in vapour scavenging during periods of particle formation. This reduction enhances the survival probability of freshly nucleated clusters by increasing vapour lifetime and reducing coagulation losses.

Reported values from polluted urban environments, such as those presented by (Gani et al., 2020; Laakso et al., 2006), span a wide range depending on pollution level and time of day, with CS values reaching ~0.14–0.17 s^{-1} under highly polluted winter evening conditions, ~0.035 s^{-1} during relatively cleaner spring daytime periods, and as low as ~0.004 s^{-1} during monsoon afternoons. In this framework, the CAS-AO site represents an intermediate regime: event-day CS values (~0.0095 s^{-1}) are comparable to cleaner urban daytime conditions, while non-event values (~0.0292 s^{-1}) approach moderately polluted regimes.

Further observations from Delhi show that NPF events are typically observed when CS remains below ~0.06 s^{-1}, despite an overall range of ~0.004–0.8 s^{-1}, indicating that only periods with sufficiently reduced sink conditions allow particle formation and sustained growth (Ali et al., 2025). The event-day CS values in this study fall well within this favourable regime, whereas non-event conditions approach this threshold, indicating a transition between conditions that permit and inhibit NPF.

Importantly, the growth rates in this study exhibit a clear size dependence. The event-wise dataset gives median values of 10.6 and 14.7 nm h^{-1} in the nominal 3-7 nm range using the appearance-time and Gaussian/mode-peak methods, respectively, and 16.8 and 19.0 nm h^{-1} in the nominal 7-20 nm range. These values are comparable to the

range of 5.7-30 nm h^{-1} reported for Delhi in previous studies under highly polluted conditions (Aliaga et al., 2023; Mönkkönen et al., 2004; Sarangi et al., 2015).

The reported CS and growth rate values at CAS-AO suggest that there exist sufficient sources of vapours that can form clusters and enable rapid growth, maintaining a sufficiently high survival probability despite the polluted background. Variable wind fields, radiation, and sink strength can disrupt the balance between vapour production and particle losses, leading to fragmented or suppressed nucleation signatures. While nucleation may still occur intermittently, the combined effect of rapid vapour removal and efficient particle scavenging strongly limits particle survival and growth. In contrast, the comparatively lower sink environment at Sonipat permits temporal windows favourable for particle survival and intermittent growth under suitable meteorological conditions.

4. Conclusion

This study presents the first systematic characterisation of size-resolved atmospheric ions and sub-10 nm particles at a suburban Indo-Gangetic Plain site (CAS-AO, Sonipat), combining NAIS and limited concurrent SMPS measurements with meteorological observations over May-December 2023 to examine the occurrence, formation, and growth of new particle formation (NPF) in a high-pollution continental environment.

NPF events occurred predominantly during summer, exceeding 85 % of valid NAIS days in May and June, while non-event conditions dominated in November and December (>85 % of valid NAIS days). Atmospheric ions in the 2-4 nm range showed modest diurnal enhancement (day/night ratio ~1.5-2.5), substantially weaker than the robust daytime increase in 3-5 nm particles (day/night ratio ~3-3.5 during summer). The presence of transported event days and this number-concentration decoupling indicate that precursor vapour availability and condensation sink both influence particle survival and growth.

Within the concurrent NAIS-SMPS subset, the event-day condensation sink at CAS-AO (0.0095 s^{-1}) was lower than the non-event median (0.0292 s^{-1}). These values fall between suppression thresholds reported for polluted environments such as Delhi and Beijing and the much lower values typical of clean environments such as boreal forest sites (~10^{-3}-10^{-2} s^{-1}). This positions CAS-AO as an intermediate-pollution environment where NPF can occur near the upper boundary of conditions permissive for cluster survival.

In this environment, however, pollution plumes, boundary layer variability, wind fluctuations, and precipitation intermittently mask or distort NPF signals introducing additional particle modes that overlap with or completely suppress the growing nucleation mode. As a result, both traditional visual classification methods and automated approaches, which were developed for cleaner environments with distinct lognormal size distributions, cannot be directly applied without careful adaptation. Growth rate estimation methods similarly assume steady-state, size-independent growth and distinct modes assumptions frequently violated here. Preprocessing and smoothing procedures, while necessary to reduce noise, risk attenuating genuine atmospheric features or retaining artefacts where signal-to-noise ratios are low. Careful day-by-day screening remained necessary even when automated frameworks were applied, and quantitative parameters such as J and GR carry increased uncertainty relative to cleaner-site applications. These methodological limitations must be explicitly acknowledged in any interpretation of NPF characteristics in such environments.

Despite these limitations, the results demonstrate frequent NPF occurrence and rapid growth in the IGP during periods with favourable conditions. The high growth rates may increase particle survival probability and can contribute to particle volume and mass if growing modes reach larger diameters; however, robust quantification of the NPF contribution to particle mass or CCN requires longer concurrent NAIS-SMPS measurements and supporting precursor-gas observations, together with a rigorous assessment of whether the observed growth rates remain representative over the time needed for particles to reach CCN-relevant sizes.

Code and data availability

The observational data from the CAS-AO atmospheric observatory (NAIS ion and total particle number size distributions, SMPS PNSD, and AWS meteorological parameters) used in this study, together with the analysis codes will be made publicly available upon acceptance of this manuscript. The dataset and code repository will be archived at Zenodo [to be confirmed upon publication] and accessible via a persistent DOI that will be provided in the final published version of this article. Readers interested in accessing the data or code prior to publication are encouraged to contact the corresponding authors.

Author contributions

GKS and SG conceptualised the study. GKS, AAW, and JR carried out the data collection. GKS and JL curated the data. GKS developed the methodology and performed the formal analysis, visualisation, and wrote the original draft of the manuscript. RKK, DG, MK, TP, PP, RCT, and SG provided resources. PP, RCT, and SG acquired funding, administered the project, and supervised the work. All authors contributed to reviewing and editing the manuscript.

Competing interests

The authors declare that they have no conflict of interest. TP is a member of the editorial board of ACP.

Acknowledgements

We would like to sincerely acknowledge Prof. Krishna Achuta Rao and Prof. Somnath Baidya Roy for their vision, leadership, and active involvement in the planning and administrative efforts that led to the establishment of the atmospheric observatory at IIT Delhi. We are also grateful to the senior administration of IIT Delhi for their continued support in building and sustaining this important scientific infrastructure. Special thanks to the Institute for Atmospheric and Earth System Research (INAR), University of Helsinki, for their collaboration and support in facilitating this research, particularly through the provision of instrumentation, technical guidance, and associated infrastructure that made key observations and analyses possible. ChatGPT (OpenAI) was used to assist with grammar, sentence structure, and language clarity during manuscript preparation. All scientific content, analysis, and interpretation were developed by the authors.

Financial support

We acknowledge financial support from the European Commission via FOCI Project (101056783), from the Research Council of Finland via Atmosphere and Climate Competence Centre (ACCC) Flagship (337549, 3570902, 359340) and via CO-ENHANCIN project (360114), Jane and Aatos Erkko Foundation and from University of Helsinki, Faculty of Science via ACTRIS-HY.

References

Aalto, P., Hämeri, K., Becker, E., Weber, R., Salm, J., Mäkelä, J. M., Hoell, C., O'dowd, C. D., Karlsson, H., Hansson, H.-C., Väkevä, M., Koponen, I. K., Buzorius, G., and Kulmala, M.: Physical characterization of aerosol particles during nucleation events, Tellus B Chem. Phys. Meteorol., 53, 344, https://doi.org/10.3402/tellusb.v53i4.17127, 2001.

Ali, U., Singh, V., Faisal, M., Kumar, M., and Gani, S.: Exploring the influence of physical and chemical factors on new particle formation in a polluted megacity, Environ. Sci. Atmos., 5, 25–47, https://doi.org/10.1039/d4ea00114a, 2025.

Aliaga, D., Tuovinen, S., Zhang, T., Lampilahti, J., Li, X., Ahonen, L., Kokkonen, T., Nieminen, T., Hakala, S., Paasonen, P., Bianchi, F., Worsnop, D., Kerminen, V.-M., and Kulmala, M.: Nanoparticle ranking analysis: determining new particle formation (NPF) event occurrence and intensity based on the concentration spectrum of formed (sub-5 nm) particles, Aerosol Res., 1, 81–92, https://doi.org/10.5194/ar-1-81-2023, 2023.

Chutia, L., Ojha, N., Girach, I., Pathak, B., Sahu, L. K., Sarangi, C., Flemming, J., Da Silva, A., and Bhuyan, P. K.: Trends in sulfur dioxide over the Indian subcontinent during 2003–2019, Atmos. Environ., 284, 119189, https://doi.org/10.1016/j.atmosenv.2022.119189, 2022.

CIMO Guide No.8, WMO,: Guide to Meteorological Instruments and Methods of Observation: (CIMO guide). 2014 edition, updated in 2017, https://doi.org/10.25607/OBP-432, 2017.

Dada, L., Chellapermal, R., Buenrostro Mazon, S., Paasonen, P., Lampilahti, J., Manninen, H. E., Junninen, H., Petäjä, T., Kerminen, V.-M., and Kulmala, M.: Refined classification and characterization of atmospheric new-particle formation events using air ions, Atmos. Chem. Phys., 18, 17883–17893, https://doi.org/10.5194/acp-18-17883-2018, 2018.

Dal Maso, M., Kulmala, M., Riipinen, I., Wagner, R., Hussein, T., Aalto, P. P., and Lehtinen, K. E. J.: Formation and growth of fresh atmospheric aerosols: eight years of aerosol size distribution data from SMEAR II, Hyytiälä, Finland, Boreal Environ. Res., 10, 323–336, 2005.

Deng, C., Cai, R., Yan, C., Zheng, J., and Jiang, J.: Formation and growth of sub-3 nm particles in megacities: impact of background aerosols, Faraday Discuss., 226, 348–363, https://doi.org/10.1039/D0FD00083C, 2021.

Ezhova, E., Kerminen, V.-M., Lehtinen, K. E. J., and Kulmala, M.: A simple model for the time evolution of the condensation sink in the atmosphere for intermediate Knudsen numbers, Atmos. Chem. Phys., 18, 2431–2442, https://doi.org/10.5194/acp-18-2431-2018, 2018.

Gagné, S., Lehtipalo, K., Manninen, H. E., Nieminen, T., Schobesberger, S., Franchin, A., Yli-Juuti, T., Boulon, J., Sonntag, A., Mirme, S., Mirme, A., Hõrrak, U., Petäjä, T., Asmi, E., and Kulmala, M.: Intercomparison of air ion spectrometers: an evaluation of results in varying conditions, Atmos. Meas. Tech., 4, 805–822, https://doi.org/10.5194/amt-4-805-2011, 2011.

Gani, S., Bhandari, S., Seraj, S., Wang, D. S., Patel, K., Soni, P., Arub, Z., Habib, G., Hildebrandt Ruiz, L., and Apte, J. S.: Submicron aerosol composition in the world's most polluted megacity: the Delhi Aerosol Supersite study, Atmos. Chem. Phys., 19, 6843–6859, https://doi.org/10.5194/acp-19-6843-2019, 2019.

Gani, S., Bhandari, S., Patel, K., Seraj, S., Soni, P., Arub, Z., Habib, G., Hildebrandt Ruiz, L., and Apte, J. S.: Particle number concentrations and size distribution in a polluted megacity: the Delhi Aerosol Supersite study, Atmos. Chem. Phys., 20, 8533–8549, https://doi.org/10.5194/acp-20-8533-2020, 2020.

Gordon, H., Kirkby, J., Baltensperger, U., Bianchi, F., Breitenlechner, M., Curtius, J., Dias, A., Dommen, J., Donahue, N. M., Dunne, E. M., Duplissy, J., Ehrhart, S., Flagan, R. C., Frege, C., Fuchs, C., Hansel, A., Hoyle, C. R., Kulmala, M., Kürten, A.,

Lehtipalo, K., Makhmutov, V., Molteni, U., Rissanen, M. P., Stozkhov, Y., Tröstl, J., Tsagkogeorgas, G., Wagner, R., Williamson, C., Wimmer, D., Winkler, P. M., Yan, C., and Carslaw, K. S.: Causes and importance of new particle formation in the present-day and preindustrial atmospheres, J. Geophys. Res. Atmos., 122, 8739–8760, https://doi.org/10.1002/2017JD026844, 2017.

Gormley, P. G. and Kennedy, M.: Diffusion from a Stream Flowing through a Cylindrical Tube, Proc. R. Ir. Acad. Sect. Math. Phys. Sci., 52, 163–169, 1949.

Guttikunda, S. K. and Gurjar, B. R.: Role of meteorology in seasonality of air pollution in megacity Delhi, India, Environ. Monit. Assess., 184, 3199–3211, https://doi.org/10.1007/s10661-011-2182-8, 2012.

Herrmann, E., Ding, A. J., Kerminen, V.-M., Petäjä, T., Yang, X. Q., Sun, J. N., Qi, X. M., Manninen, H., Hakala, J., Nieminen, T., Aalto, P. P., Kulmala, M., and Fu, C. B.: Aerosols and nucleation in eastern China: first insights from the new SORPES-NJU station, Atmos. Chem. Phys., 14, 2169–2183, https://doi.org/10.5194/acp-14-2169-2014, 2014.

Hinds, W. C. and Zhu, Y.: Aerosol technology: properties, behavior, and measurement of airborne particles, Third edition., Wiley, Hoboken, NJ, 425 pp., 2022.

Iida, K., Stolzenburg, M. R., McMurry, P. H., and Smith, J. N.: Estimating nanoparticle growth rates from size-dependent charged fractions: Analysis of new particle formation events in Mexico City, J. Geophys. Res. Atmos., 113, 2007JD009260, https://doi.org/10.1029/2007JD009260, 2008.

Johnson, T. J., Nishida, R. T., Irwin, M., Symonds, J. P. R., Olfert, J. S., and Boies, A. M.: Measuring the bipolar charge distribution of nanoparticles: Review of methodologies and development using the Aerodynamic Aerosol Classifier, J. Aerosol Sci., 143, 105526, https://doi.org/10.1016/j.jaerosci.2020.105526, 2020.

Kanawade, V. P., Sebastian, M., Hooda, R. K., and Hyvärinen, A.-P.: Atmospheric new particle formation in India: Current understanding and knowledge gaps, Atmos. Environ., 270, 118894, https://doi.org/10.1016/j.atmosenv.2021.118894, 2022.

Kangasluoma, J., Cai, R., Jiang, J., Deng, C., Stolzenburg, D., Ahonen, L. R., Chan, T., Fu, Y., Kim, C., Laurila, T. M., Zhou, Y., Dada, L., Sulo, J., Flagan, R. C., Kulmala, M., Petäjä, T., and Lehtipalo, K.: Overview of measurements and current instrumentation for 1–10 nm aerosol particle number size distributions, J. Aerosol Sci., 148, 105584, https://doi.org/10.1016/j.jaerosci.2020.105584, 2020.

Kerminen, V.-M., Chen, X., Vakkari, V., Petäjä, T., Kulmala, M., and Bianchi, F.: Atmospheric new particle formation and growth: review of field observations, Environ. Res. Lett., 13, 103003, https://doi.org/10.1088/1748-9326/aadf3c, 2018.

Kirkby, J., Duplissy, J., Sengupta, K., Frege, C., Gordon, H., Williamson, C., Heinritzi, M., Simon, M., Yan, C., Almeida, J., Tröstl, J., Nieminen, T., Ortega, I. K., Wagner, R., Adamov, A., Amorim, A., Bernhammer, A.-K., Bianchi, F., Breitenlechner, M., Brilke, S., Chen, X., Craven, J., Dias, A., Ehrhart, S., Flagan, R. C., Franchin, A., Fuchs, C., Guida, R., Hakala, J., Hoyle, C. R., Jokinen, T., Junninen, H., Kangasluoma, J., Kim, J., Krapf, M., Kürten, A., Laaksonen, A., Lehtipalo, K., Makhmutov, V., Mathot, S., Molteni, U., Onnela, A., Peräkylä, O., Piel, F., Petäjä, T., Praplan, A. P., Pringle, K., Rap, A., Richards, N. A. D., Riipinen, I., Rissanen, M. P., Rondo, L., Sarnela, N., Schobesberger, S., Scott, C. E., Seinfeld, J. H., Sipilä, M., Steiner, G., Stozhkov, Y., Stratmann, F., Tomé, A., Virtanen, A., Vogel, A. L., Wagner, A. C., Wagner, P. E., Weingartner, E., Wimmer, D., Winkler, P. M., Ye, P., Zhang, X., Hansel, A., Dommen, J., Donahue, N. M., Worsnop, D. R., Baltensperger, U., Kulmala, M., Carslaw, K. S., and Curtius, J.: Ion-induced nucleation of pure biogenic particles, Nature, 533, 521–526, https://doi.org/10.1038/nature17953, 2016.

Kontkanen, J., Järvinen, E., Manninen, H. E., Lehtipalo, K., Kangasluoma, J., Decesari, S., Gobbi, G. P., Laaksonen, A., Petäjä, T., and Kulmala, M.: High concentrations of sub-3nm clusters and frequent new particle formation observed in the Po Valley,

Italy, during the PEGASOS 2012 campaign, Atmos. Chem. Phys., 16, 1919–1935, https://doi.org/10.5194/acp-16-1919-2016, 2016.

Kulmala, M. and Laaksonen, A.: Binary nucleation of water–sulfuric acid system: Comparison of classical theories with different H2SO4 saturation vapor pressures, J. Chem. Phys., 93, 696–701, https://doi.org/10.1063/1.459519, 1990.

Kulmala, M., Laakso, L., Lehtinen, K. E. J., Riipinen, I., Dal Maso, M., Anttila, T., Kerminen, V.-M., Hõrrak, U., Vana, M., and Tammet, H.: Initial steps of aerosol growth, Atmos. Chem. Phys., 4, 2553–2560, https://doi.org/10.5194/acp-4-2553-2004, 2004.

Kulmala, M., Riipinen, I., Sipilä, M., Manninen, H. E., Petäjä, T., Junninen, H., Dal Maso, M., Mordas, G., Mirme, A., Vana, M., Hirsikko, A., Laakso, L., Harrison, R. M., Hanson, I., Leung, C., Lehtinen, K. E. J., and Kerminen, V.-M.: Toward Direct Measurement of Atmospheric Nucleation, Science, 318, 89–92, https://doi.org/10.1126/science.1144124, 2007.

Kulmala, M., Petäjä, T., Nieminen, T., Sipilä, M., Manninen, H. E., Lehtipalo, K., Dal Maso, M., Aalto, P. P., Junninen, H., Paasonen, P., Riipinen, I., Lehtinen, K. E. J., Laaksonen, A., and Kerminen, V.-M.: Measurement of the nucleation of atmospheric aerosol particles, Nat. Protoc., 7, 1651–1667, https://doi.org/10.1038/nprot.2012.091, 2012.

Kulmala, M., Kerminen, V.-M., Petäjä, T., Ding, A. J., and Wang, L.: Atmospheric gas-to-particle conversion: why NPF events are observed in megacities?, Faraday Discuss., 200, 271–288, https://doi.org/10.1039/C6FD00257A, 2017.

Kulmala, M., Aliaga, D., Tuovinen, S., Cai, R., Junninen, H., Yan, C., Bianchi, F., Cheng, Y., Ding, A., Worsnop, D. R., Petäjä, T., Lehtipalo, K., Paasonen, P., and Kerminen, V.-M.: Opinion: A paradigm shift in investigating the general characteristics of atmospheric new particle formation using field observations, Aerosol Res., 2, 49–58, https://doi.org/10.5194/ar-2-49-2024, 2024.

Laakso, L., Koponen, I. K., Mönkkönen, P., Kulmala, M., Kerminen, V.-M., Wehner, B., Wiedensohler, A., Wu, Z., and Hu, M.: Aerosol particles in the developing world; a comparison between New Delhi in India and Beijing in China, Water. Air. Soil Pollut., 173, 5–20, https://doi.org/10.1007/s11270-005-9018-5, 2006.

Lampilahti, J., Paasonen, P., Tuovinen, S., Lehtipalo, K., Kerminen, V.-M., and Kulmala, M.: A cross-correlation-based method for determining size-resolved particle growth rates, Aerosol Res., 3, 637–647, https://doi.org/10.5194/ar-3-637-2025, 2025.

Lehtinen, K. E. J., Dal Maso, M., Kulmala, M., and Kerminen, V.-M.: Estimating nucleation rates from apparent particle formation rates and vice versa: Revised formulation of the Kerminen–Kulmala equation, J. Aerosol Sci., 38, 988–994, https://doi.org/10.1016/j.jaerosci.2007.06.009, 2007.

Lehtipalo, K., Leppä, J., Kontkanen, J., Kangasluoma, J., Franchin, A., Wimmer, D., Schobesberger, S., Junninen, H., Petäjä, T., Sipilä, M., Mikkilä, J., Vanhanen, J., Worsnop, D. R., and Kulmala, M.: Methods for determining particle size distribution and growth rates between 1 and 3 nm using the Particle Size Magnifier, Boreal Environ. Res., 19, 22, 2014.

Leppä, J., Mui, W., Grantz, A. M., and Flagan, R. C.: Charge distribution uncertainty in differential mobility analysis of aerosols, Aerosol Sci. Technol., 51, 1168–1189, https://doi.org/10.1080/02786826.2017.1341039, 2017.

Manninen, H. E., Nieminen, T., Asmi, E., Gagné, S., Häkkinen, S., Lehtipalo, K., Aalto, P., Vana, M., Mirme, A., Mirme, S., Hõrrak, U., Plass-Dülmer, C., Stange, G., Kiss, G., Hoffer, A., Törő, N., Moerman, M., Henzing, B., De Leeuw, G., Brinkenberg, M., Kouvarakis, G. N., Bougiatioti, A., Mihalopoulos, N., O'Dowd, C., Ceburnis, D., Arneth, A., Svenningsson, B., Swietlicki, E., Tarozzi, L., Decesari, S., Facchini, M. C., Birmili, W., Sonntag, A., Wiedensohler, A., Boulon, J., Sellegri, K., Laj, P., Gysel, M., Bukowiecki, N., Weingartner, E., Wehrle, G., Laaksonen, A., Hamed, A., Joutsensaari, J., Petäjä, T.,

Kerminen, V.-M., and Kulmala, M.: EUCAARI ion spectrometer measurements at 12 European sites – analysis of new particle formation events, Atmos. Chem. Phys., 10, 7907–7927, https://doi.org/10.5194/acp-10-7907-2010, 2010.

Manninen, H. E., Franchin, A., Schobesberger, S., Hirsikko, A., Hakala, J., Skromulis, A., Kangasluoma, J., Ehn, M., Junninen, H., Mirme, A., Mirme, S., Sipilä, M., Petäjä, T., Worsnop, D. R., and Kulmala, M.: Characterisation of corona-generated ions used in a Neutral cluster and Air Ion Spectrometer (NAIS), Atmos. Meas. Tech., 4, 2767–2776, https://doi.org/10.5194/amt-4-2767-2011, 2011.

Manninen, H. E., Mirme, S., Mirme, A., Petäjä, T., and Kulmala, M.: How to reliably detect molecular clusters and nucleation mode particles with Neutral cluster and Air Ion Spectrometer (NAIS), Aerosols/In Situ Measurement/Validation and Intercomparisons, https://doi.org/10.5194/amt-2016-25, 2016.

Mirme, S. and Mirme, A.: The mathematical principles and design of the NAIS – a spectrometer for the measurement of cluster ion and nanometer aerosol size distributions, Atmos. Meas. Tech., 6, 1061–1071, https://doi.org/10.5194/amt-6-1061-2013, 2013.

Mönkkönen, P., Koponen, I. K., Lehtinen, K. E. J., Hämeri, K., Uma, R., and Kulmala, M.: Measurements in a highly polluted Asian mega city: observations of aerosol number size distribution, modal parameters and nucleation events, https://doi.org/10.5194/acpd-4-5407-2004, 17 September 2004.

Paasonen, P., Peltola, M., Kontkanen, J., Junninen, H., Kerminen, V.-M., and Kulmala, M.: Comprehensive analysis of particle growth rates from nucleation mode to cloud condensation nuclei in boreal forest, Atmos. Chem. Phys., 18, 12085–12103, https://doi.org/10.5194/acp-18-12085-2018, 2018.

Pawar, P. V., Ghude, S. D., Govardhan, G., Acharja, P., Kulkarni, R., Kumar, R., Sinha, B., Sinha, V., Jena, C., Gunwani, P., Adhya, T. K., Nemitz, E., and Sutton, M. A.: Chloride (HCl/Cl^-) dominates inorganic aerosol formation from ammonia in the Indo-Gangetic Plain during winter: modeling and comparison with observations, Atmos. Chem. Phys., 23, 41–59, https://doi.org/10.5194/acp-23-41-2023, 2023.

Pirjola, L., Kulmala, M., Wilck, M., Bischo, A., Stratmann, F., and Otto, E.: Formation of sulphuric acid aerosols and cloud condensation nuclei: An expression for significant nucleation and model comparison, J Aerosol Sci, 30, 1079–1094, 1999.

Rathore, J., Ganguly, D., Singh, V., Gupta, M., Vazhathara, V. J., Biswal, A., Kunchala, R. K., Patra, P. K., Sahu, L. K., Gani, S., and Dey, S.: Characteristics of Haze Pollution Events During Biomass Burning Period at an Upwind Site of Delhi, J. Geophys. Res. Atmos., 130, e2024JD042347, https://doi.org/10.1029/2024JD042347, 2025.

Sarangi, B., Aggarwal, S. G., and Gupta, P. K.: A Simplified Approach to Calculate Particle Growth Rate Due to Self-Coagulation, Scavenging and Condensation Using SMPS Measurements during a Particle Growth Event in New Delhi, Aerosol Air Qual. Res., 15, 166–179, https://doi.org/10.4209/aaqr.2013.12.0350, 2015.

Sebastian, M., Kompalli, S. K., Kumar, V. A., Jose, S., Babu, S. S., Pandithurai, G., Singh, S., Hooda, R. K., Soni, V. K., Pierce, J. R., Vakkari, V., Asmi, E., Westervelt, D. M., Hyvärinen, A.-P., and Kanawade, V. P.: Observations of particle number size distributions and new particle formation in six Indian locations, Atmos. Chem. Phys., 22, 4491–4508, https://doi.org/10.5194/acp-22-4491-2022, 2022.

Seinfeld, J. H.: Atmospheric Chemistry and Physics: From Air Pollution to Climate Change, 1st ed., John Wiley & Sons, Incorporated, Newark, 1 pp., 2016.

Sellegri, K., Rose, C., Marinoni, A., Lupi, A., Wiedensohler, A., Andrade, M., Bonasoni, P., and Laj, P.: New Particle Formation: A Review of Ground-Based Observations at Mountain Research Stations, Atmosphere, 10, 493, https://doi.org/10.3390/atmos10090493, 2019.

Singh, N., Dey, S., and Knibbs, L. D.: Spatio-temporal patterns of tropospheric NO2 over India during 2005–2019, Atmos. Pollut. Res., 14, 101692, https://doi.org/10.1016/j.apr.2023.101692, 2023.

Stolzenburg, D., Cai, R., Blichner, S. M., Kontkanen, J., Zhou, P., Makkonen, R., Kerminen, V.-M., Kulmala, M., Riipinen, I., and Kangasluoma, J.: Atmospheric nanoparticle growth, Rev. Mod. Phys., 95, 045002, https://doi.org/10.1103/RevModPhys.95.045002, 2023.

Stolzenburg, M. R. and McMurry, P. H.: Method to assess performance of scanning mobility particle sizer (SMPS) instruments and software, Aerosol Sci. Technol., 52, 609–613, https://doi.org/10.1080/02786826.2018.1455962, 2018.

Tammet, H.: Size and mobility of nanometer particles, clusters and ions, J. Aerosol Sci., 26, 459–475, https://doi.org/10.1016/0021-8502(94)00121-E, 1995.

Tomasi, C. and Lupi, A.: Primary and Secondary Sources of Atmospheric Aerosol, in: Atmospheric Aerosols, edited by: Tomasi, C., Fuzzi, S., and Kokhanovsky, A., Wiley, 1–86, https://doi.org/10.1002/9783527336449.ch1, 2017.

Trivedi, D. K., Ali, K., and Beig, G.: Impact of meteorological parameters on the development of fine and coarse particles over Delhi, Sci. Total Environ., 478, 175–183, https://doi.org/10.1016/j.scitotenv.2014.01.101, 2014.

Wagner, R., Manninen, H. E., Franchin, A., Lehtipalo, K., Mirme, S., Steiner, G., Petäjä, T., and Kulmala, M.: On the accuracy of ion measurements using a neutral cluster and air ion spectrometer, BOREAL Environ. Res., 21, 230–241, https://doi.org/10.60910/XR8J-5A1A, 2016.

Wang, T., Song, Y., Xu, Z., Liu, M., Xu, T., Liao, W., Yin, L., Cai, X., Kang, L., Zhang, H., and Zhu, T.: Why is the Indo-Gangetic Plain the region with the largest NH_3 column in the globe during pre-monsoon and monsoon seasons?, Atmos. Chem. Phys., 20, 8727–8736, https://doi.org/10.5194/acp-20-8727-2020, 2020.

Yli-Juuti, T., Nieminen, T., Hirsikko, A., Aalto, P. P., Asmi, E., Hõrrak, U., Manninen, H. E., Patokoski, J., Dal Maso, M., Petäjä, T., Rinne, J., Kulmala, M., and Riipinen, I.: Growth rates of nucleation mode particles in Hyytiälä during 2003−2009: variation with particle size, season, data analysis method and ambient conditions, Atmos. Chem. Phys., 11, 12865–12886, https://doi.org/10.5194/acp-11-12865-2011, 2011.

Yu, M., Tang, G., Yang, Y., Li, Q., Wang, Y., Miao, S., Zhang, Y., and Wang, Y.: The interaction between urbanisation and aerosols during a typical winter haze event in Beijing, Atmos. Chem. Phys., 20, 9855–9870, https://doi.org/10.5194/acp-20-9855-2020, 2020.